RSC Advances

PAPER

View Article Online
View Journal | View Issue

Cite this: *RSC Adv.*, 2025, **15**, 777

Preparation and characterization of Ru-TiO_2/PC/Fe_3O_4 composite catalyst with enhanced photocatalytic performance and magnetic recoverability under simulated solar light

Ruixiang Wu, *[ab] Hanyan Zhang,[c] Wenhua Liu,[b] Renao Bai,[a] Delun Zheng,[a] Xiufang Tian,*[a] Weikai Lin,[b] Lejian Li[a] and Qianwei Ke[a]

Received 29th October 2024
Accepted 23rd December 2024

DOI: 10.1039/d4ra07712a

rsc.li/rsc-advances

This research focuses on the development of a novel Ru-doped TiO_2/grapefruit peel biochar/Fe_3O_4 (Ru-TiO_2/PC/Fe_3O_4) composite catalyst, which exhibits exceptional photocatalytic efficacy under simulated solar light irradiation. The catalyst is highly effective in the degradation of rhodamine B (RhB), methylene blue (MB), methyl orange (MO), as well as actual industrial dye wastewater (IDW), and can be recovered magnetically for multiple reuse cycles. Significantly, the PCTRF-100 sample exhibited degradation efficiencies of 99.4% for RhB and 99.8% for MB within 60 min, and 98.04% for MO within 120 min. In the case of actual dye wastewater, a reduction in chemical oxygen demand from 1540 mg L^{-1} to 784 mg L^{-1} was achieved within 300 min, corresponding to a degradation rate of 46.81%. The remarkable photocatalytic activity observed is primarily attributed to the synergistic interactions among Ru-TiO_2, biochar, and Fe_3O_4, which effectively facilitate the separation and migration of electron–hole pairs in TiO_2.

1 Introduction

The swift advancement of modern agriculture and industry has led to an enhancement in living standards. Nevertheless, this progress has concurrently exacerbated environmental pollution, particularly water pollution, which has emerged as a significant environmental and social challenge.[1–3] Wastewater containing colored dyes, released from industries such as textiles, printing, papermaking, and coatings, encompasses toxic, carcinogenic, and teratogenic substances. Inadequate treatment of such wastewater can result in profound ecological damage.[4,5] As a result, the development of efficient and environmentally sustainable technologies to reduce these pollutants has become a major research focus within the environmental field. Presently, methods such as adsorption, Fenton technology, advanced oxidation processes, and photocatalysis are extensively employed for the treatment of dye wastewater.[6–8] Among these methods, photocatalytic technology is regarded as the most promising green technology for environmental protection due to its ecological compatibility, high efficiency, and cost-effectiveness.[9,10]

The foundation of photocatalytic technology is the development of catalysts that are both efficient and environmentally benign. At present, materials such as TiO_2, ZnO, and CdS are extensively utilized as photocatalysts,[11–13] with TiO_2 being regarded as the most promising due to its non-toxic nature, low cost, superior physicochemical properties, and high stability.[14] Nonetheless, TiO_2 suffers from limitations, including low visible light utilization,[15] a high rate of electron–hole recombination,[16] and challenges associated with separation and recovery,[17,18] which constrain its practical applications. To address these drawbacks, our research team has successfully synthesized gradient porous TiO_2 (ref. 19) and TiO_2/grapefruit peel (GP) biochar composite materials,[20] employing GP as a biological template and carbon source, which has significantly enhanced photocatalytic performance. However, the issues of limited visible light utilization and difficulty in separation and recovery persist. Research indicates that doping with transition metals, such as Ru, can substantially improve the visible light activity of TiO_2. For instance, Kulkarni *et al.*[21] synthesized Ru/TiO_2 composites using an impregnation technique, which demonstrated considerable activity in the catalytic degradation of benzyl butyl phthalate. Elsalamony *et al.*[22] prepared Ru/TiO_2 photocatalysts through impregnation, markedly enhancing the catalytic degradation performance of 2-chlorophenol under visible light. Additionally, Zhang *et al.*[23] developed Ru-doped TiO_2 spheres, which exhibited strong photocatalytic hydrogen production performance under visible light conditions.

[a]*College of Construction and Ecology, Shantou Polytechnic, Shantou 515078, Guangdong, China. E-mail: rxwu@stpt.edu.cn; xftian@stpt.edu.cn*

[b]*Guangdong Provincial Laboratory of Marine Biotechnology, Institute of Marine Sciences, Shantou University, Shantou 515063, Guangdong, China*

[c]*Shantou Goworld Display Co. Ltd, LongJiang Road No. 12, ShanTou 515043, Guangdong, China*

Nevertheless, these studies did not resolve the challenge of separation and recovery. It has been established that TiO_2 composite catalysts, when combined with magnetic materials, can be swiftly separated and recovered using an external magnetic field, thereby improving their practicality.[24,25] For example, Niu *et al.*[26] designed a core–shell structured Fe_3O_4@-TiO_2 photocatalyst, which displayed high catalytic activity for the degradation of neutral red in aqueous solution under visible light and could be easily recovered with a magnet. Similarly, Zhang *et al.*[27] synthesized Fe_3O_4@C@Ru composites *via* a three-step method, and Rajabathar *et al.*[28] prepared Fe_3O_4/TiO_2 composites using a hydrothermal synthesis method. Both catalysts achieved degradation rates exceeding 90% for MB under simulated solar light and could be effectively reused through magnetic separation.

Building upon prior research, a Ru-TiO_2/PC/Fe_3O_4 composite catalyst was successfully synthesized utilizing a low-temperature hydrothermal method. This composite exhibited high efficiency in the degradation of RhB, MB, MO, and IDW under simulated solar light conditions, while also offering magnetic separation capabilities. A comprehensive examination of its synthesis process, photocatalytic efficiency, underlying mechanisms, and facile separation and recovery methods is crucial for advancing its practical applications.

2 Materials and methods

2.1 Materials

Grapefruit peels were purchased from Shantou Agricultural and Trade Market, Shantou, China. The following chemicals were utilized: tetrabutyl titanate(TBOT)(500 mL, AR), RhB (100 g, AR), $RuCl_3$ (1 g, AR), $FeCl_2 \cdot 4H_2O$ (5 g, AR), $FeCl_3 \cdot 6H_2O$ (5 g, AR), MB (100 g, AR) and MO (100 g, AR) acquired from Shanghai Macklin Company Limited; as well as potassium hydroxide (500 g, AR), anhydrous ethanol (500 mL, AR) and acetic acid (500 mL, AR), $NH_3 \cdot H_2O$ (500 mL, AR) both procured from Sinopharm Chemical Reagent Co., Ltd.

2.2 Preparation of Ru-TiO_2/PC/Fe_3O_4

2.2.1 Preparation of Ru-TiO_2/PC. Initially, the outer layer of the GP was removed after thorough washing, preserving only the spongy inner layer, which was subsequently cut into small pieces. These pieces were then immersed in a 0.1 mol per L NaOH solution for 12 h to modify the pore structure, followed by rinsing with water until a neutral pH was achieved, drying, and grinding to produce GP powder. Subsequently, two separate solutions were prepared: Solution A (containing 40 mL of absolute ethanol, 10 mL of TBOT, and 10 mL of glacial acetic acid) and Solution B (comprising 40 mL of absolute ethanol and 20 mL of a 1 mg per mL $RuCl_3$ alcoholic solution). Solution B was gradually added to Solution A under continuous stirring for 2 h, after which 2 g of GP powder was incorporated and subjected to rotary impregnation for 12 h. The resulting mixture was dried and then heated to 400 °C in an air atmosphere for 3 h, followed by further heating to 550 °C under a nitrogen atmosphere for an additional 3 h. The material was allowed to cool naturally to room temperature, resulting in the formation of the Ru-TiO_2/PC composite material.

2.2.2 Preparation of Fe_3O_4/PC. Based on the method described in the reference and improved,[29] the Fe_3O_4/GP biochar composite (Fe_3O_4/PC) was synthesized using a low-temperature pyrolysis technique. Initially, $FeCl_3 \cdot 6H_2O$ and $FeCl_2 \cdot 4H_2O$ were combined in a 2 : 1 molar ratio and dissolved in 100 mL of ultrapure water, to which 2.0 g of pretreated GP powder was added in a rotary evaporator. The system was maintained under a vacuum of −0.09 MPa, with a rotation speed of 180 rpm, for a vacuum rotary impregnation period of 12 h. Subsequently, 100 mL of ammonia solution was introduced to the mixture to promote the formation of Fe_3O_4. The Fe_3O_4-loaded GP powder was then separated by magnetic means and washed until the pH reached neutral (pH 7), followed by vacuum drying at 60 °C for 4 h. Finally, the dried material was placed in a tube furnace and subjected to heating at 400 °C under a nitrogen atmosphere for 2 h, after which it was allowed to cool naturally to room temperature, resulting in the formation of the Fe_3O_4/PC composite material.

2.2.3 Preparation of Ru-TiO_2/PC/Fe_3O_4. The Ru-TiO_2/PC/Fe_3O_4 composite material was synthesized employing a low-temperature hydrothermal technique. Initially, 50 mL of absolute ethanol was introduced into each of two beakers, labeled A and B. In beaker A, 500 mg of Ru-TiO_2/PC powder was added and ultrasonically dispersed for 1 h to obtain suspension A. Subsequently, based on the mass ratios of Fe_3O_4/PC to Ru-TiO_2/PC of 1 : 50, 1 : 20, 1 : 10, 1 : 5, 1 : 2, and 1 : 1, various amounts of Fe_3O_4/PC, ranging from 10 mg to 500 mg, were introduced into beaker B and ultrasonically dispersed for 1 h to form suspension B. Suspension B was then combined with suspension A, thoroughly mixed, and subjected to an additional hour of ultrasonic treatment. The resulting mixture was transferred to a reaction vessel and heated at 140 °C for 6 h in a forced-air drying oven. Following the reaction, the mixture was allowed to cool naturally, then subjected to centrifugation, filtration, and washing. The final product was vacuum-dried at 60 °C for 4 h, yielding a series of Ru-TiO_2/PC/Fe_3O_4 composite materials. These were designated as PCTRF-*x*, where *x* corresponds to the mass of Fe_3O_4/PC incorporated. The resulting samples were labeled as PCTRF-10, PCTRF-25, PCTRF-50, PCTRF-100, PCTRF-250, and PCTRF-500, while the Ru-TiO_2/PC sample without Fe_3O_4/PC addition was labeled as PCTRF-0.

2.3 Photocatalytic performance evaluation

The photocatalytic performance of the Ru-TiO_2/PC/Fe_3O_4 composite material was rigorously assessed using a 600 W xenon lamp (equipped with a solar light filter) as the illumination source, with RhB, MB, and MO solutions serving as simulants for organic dye wastewater. The capability of the composite in the treatment of actual IDW was also investigated. The experimental procedure was as follows: 100 mL of a dye solution at a concentration of 10 mg L^{-1} and 50 mg of the composite catalyst were introduced into a quartz reactor. The mixture was stirred in darkness for 30 to 60 min to achieve adsorption equilibrium. Subsequently, the xenon lamp and

a circulating water cooling system were activated, with a maintained distance of 15 cm between the light source and the liquid surface, allowing the photocatalytic reaction to proceed under continuous stirring. Throughout the experiment, 5 mL of the supernatant was periodically withdrawn from the solution, filtered through a 0.45-micron membrane, and its absorbance was measured to determine the concentration until the experiment was completed. The relationship between C/C_0 and time (t) was plotted, and the pollutant removal efficiency as well as the catalyst recovery rate were calculated according to eqn (1) and (2):

$$\eta = 1 - \frac{C}{C_0} \times 100\% \quad (1)$$

where η represents the removal rate of the dye solution (%), C_0 represents the initial concentration (mol L^{-1}), and C represents the concentration (mol L^{-1}) after reaction time t.

$$R = \frac{m}{m_0} \times 100\% \quad (2)$$

where R represents the recovery rate of the catalyst (%), m_0 represents the mass of the original catalyst (mg), and m represents the mass of the recovered catalyst (mg).

To evaluate the recyclability performance of the catalyst, the used catalyst is initially separated and recovered through magnetic methods, followed by subsequent washing and drying procedures. The treated catalyst is then reutilized in the subsequent photocatalytic experiments. This cycle is repeated multiple times to thoroughly assess the recyclability performance of the catalyst.

To ensure the reliability and reproducibility of the experimental results, each experiment was performed in triplicate ($n = 3$). The results were presented as mean ± standard deviation (SD) to clearly demonstrate the data distribution characteristics. One-way analysis of variance (ANOVA) was conducted to analyze the results of different treatment groups, with the significance level set at $p < 0.05$. Tukey's post hoc test was employed for mean separation to identify significant differences among treatment groups.

3 Results and discussion

3.1 Structural analysis of Ru-TiO_2/PC/Fe_3O_4

To examine the crystal structure and phase composition of the Fe_3O_4/PC and Ru-TiO_2/PC/Fe_3O_4 series samples, X-ray diffraction (XRD) analysis was performed, as depicted in Fig. 1a. The XRD pattern of the Fe_3O_4/PC sample reveals diffraction peaks at $2\theta = 30.08°$, 35.63°, 43.05°, 53.41°, 56.94°, 62.52°, and 73.96°, which correspond to the tetragonal crystal system of magnetite (PDF #88-0866). These peaks align with the (220), (311), (400), (442), (511), (440), and (533) crystal planes.[30,31] The Ru-TiO_2/PC/Fe_3O_4 series samples exhibit diffraction peaks at $2\theta = 25.26°$, 37.82°, 48.03°, 53.91°, 55.03°, 62.68°, 68.83°, 70.25°, and 75.14°, matching the standard diffraction peaks of anatase TiO_2 (PDF #86-1157), specifically the (101), (004), (200), (105), (211), (204), (116), (220), and (215) crystal planes.[32,33] This observation confirms that the titanium dioxide in the Ru-TiO_2/PC/Fe_3O_4 samples retains its anatase structure. Additionally, no diffraction peaks for Ru are detected, which could be due to the homogeneous distribution of Ru within TiO_2 at low concentrations, resulting in the formation of discrete compounds.[34,35] As the Fe_3O_4/PC content increases, the characteristic diffraction peaks of Fe_3O_4 become more pronounced in the XRD patterns of Ru-TiO_2/PC/Fe_3O_4. Furthermore, the absence of characteristic peaks associated with biochar may be attributed to its amorphous nature or the potential masking of its peaks by the prominent peaks of TiO_2 and Fe_3O_4. This phenomenon will be further investigated using Raman spectroscopy in subsequent analyse.

Raman spectroscopy is considered an optimal technique for characterizing the structural properties of carbon materials. In this study, Raman spectroscopic analysis was carried out on Fe_3O_4/PC, Ru-TiO_2/PC (PCTRF-0), and Ru-TiO_2/PC/Fe_3O_4 (PCTRF-100) samples. The results, as illustrated in Fig. 1b, demonstrate that all three samples displayed the characteristic peaks of graphitic carbon at approximately 1580 cm^{-1} and 1370 cm^{-1}, corresponding to the G-band and D-band, respectively.[36] The G-band is indicative of the degree of graphitization, whereas the D-band signifies the presence of defects and structural disorder within the material.[37,38] The degree of disorder and graphitization of the samples was assessed by fitting and calculating the peak area ratio R (I_D/I_G ratio). A higher R-value suggests a greater degree of disorder in the material, while a lower R-value signifies a higher degree of graphitization.[39] The calculated R values for Fe_3O_4/PC, Ru-TiO_2/PC, and Ru-TiO_2/PC/Fe_3O_4 were 1.03, 0.95, and 0.98, respectively, confirming the presence of graphitic carbon in all three samples.

To gain a more profound understanding of the porous structure of the material, nitrogen adsorption–desorption isotherms were measured using an automatic specific surface area analyzer, allowing for the estimation of key parameters such as surface area, pore volume, and pore size. The results are presented in Fig. 1c, d and Table 1. As illustrated in Fig. 1c, the N_2 adsorption–desorption isotherms of Fe_3O_4/PC and Ru-TiO_2/PC/Fe_3O_4 series samples conform to the International Union of Pure and Applied Chemistry type IV curve, which suggests a mesoporous structure with pore diameters ranging from 2 nm to 50 nm.[39] In the relative pressure range of $P/P_0 = 0.4$–1.0, H3-type hysteresis loops were observed, which are typically associated with slit-like or interlayer pores,[29] indicating the possible presence of such pores in the samples. Fig. 1d reveals that the Fe_3O_4/PC sample exhibits a bimodal Barrett–Joyner–Halenda pore size distribution, with a primary peak around 14 nm and a secondary peak between 30–60 nm. This suggests that the pores in the Fe_3O_4/PC sample are predominantly mesopores, with a minor presence of macropores. The pore sizes of the Ru-TiO_2/PC/Fe_3O_4 series samples are mainly distributed between 10–30 nm. Table 1 provides detailed information on the specific surface area, pore volume, and average pore diameter of these samples. The data indicate that the Fe_3O_4/PC sample possesses a relatively large specific surface area, pore volume, and average pore diameter. For the Ru-TiO_2/PC/Fe_3O_4 composite materials, the specific surface area and pore volume initially increase and

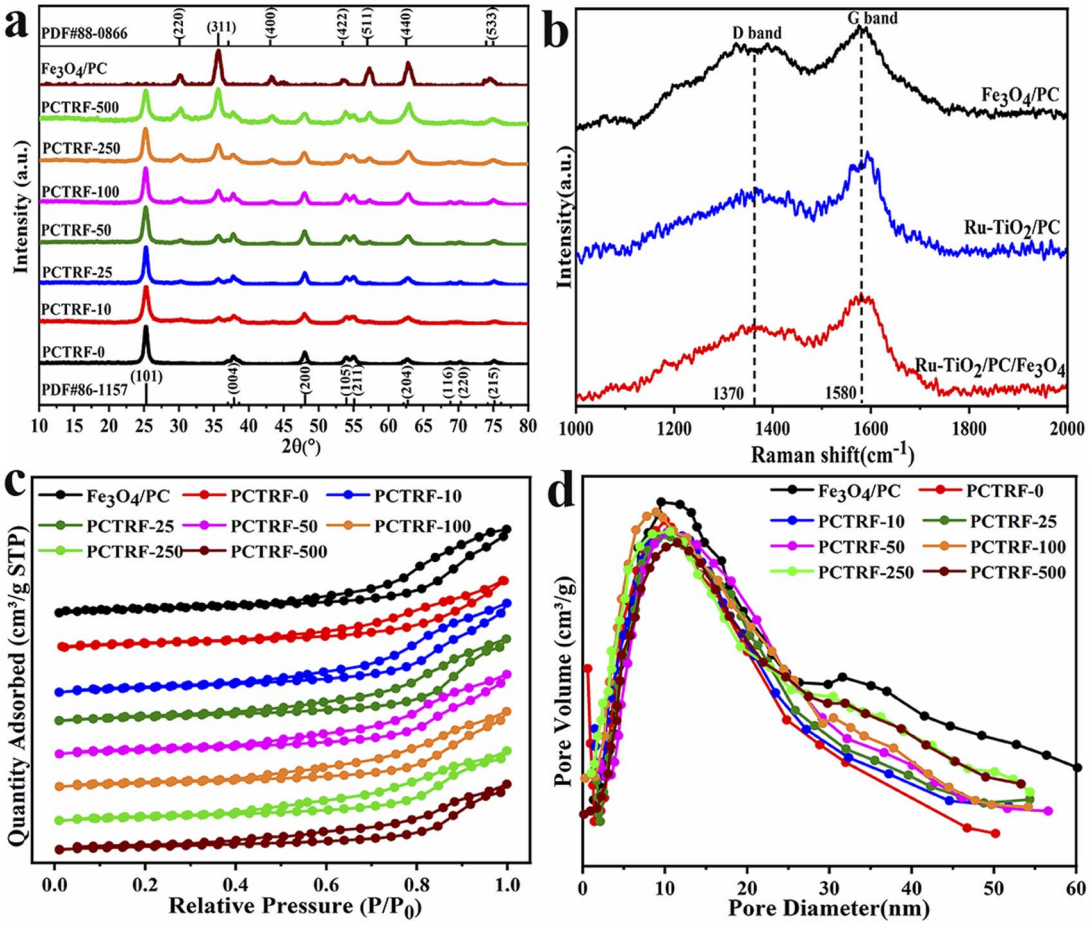

Fig. 1 (a) XRD patterns, (b) Raman spectra, (c) nitrogen adsorption–desorption isotherms, and (d) pore size distribution curves of Fe_3O_4/PC and Ru-TiO_2/PC/Fe_3O_4 series samples.

then decrease with the addition of more Fe_3O_4/PC. This finding implies that an optimal proportion of Fe_3O_4/PC promotes the formation of materials with larger specific surface areas, whereas excessive content causes aggregation and pore blockage, reducing pore structure and volume.

From the data in Table 1, it is evident that among the Ru-TiO_2/PC/Fe_3O_4 series samples, PCTRF-100 exhibits the largest specific surface area, pore volume, and average pore diameter. It has been reported that a larger surface area in photocatalytic materials correlates with more active sites, which is essential for enhancing photocatalytic performance.[35] Therefore, the PCTRF-100 sample shows potential as an effective photocatalyst.

Table 1 Surface area, pore volume, and average pore diameter of Fe_3O_4/PC and Ru-TiO_2/PC/Fe_3O_4 series samples

Materials	Surface area ($m^2\ g^{-1}$)	Pore volume ($cm^3\ g^{-1}$)	Average pore diameter (nm)
Fe_3O_4/PC	123.72	0.26	16.48
PCTRF-0	110.03	0.20	13.42
PCTRF-10	111.21	0.22	13.73
PCTRF-25	113.46	0.23	14.14
PCTRF-50	115.61	0.24	14.87
PCTRF-100	117.86	0.25	15.29
PCTRF-250	112.24	0.21	13.81
PCTRF-500	108.62	0.19	13.07

3.2 Surface elemental analysis of Ru-TiO_2/PC/Fe_3O_4

The chemical composition, elemental chemical states, and surface electron distribution of the Ru-TiO_2/PC/Fe_3O_4 sample were analyzed using X-ray photoelectron spectroscopy (XPS). The findings are presented in Fig. 2 and Table 2.

Fig. 2a illustrates the XPS survey spectrum of Ru-TiO_2/PC/Fe_3O_4. Observed at 530.60 eV, 458.44 eV, 285.04 eV, 710.99 eV, 293.36 eV, and 133.19 eV are the characteristic peaks of O 1s, Ti 2p and Ru 3p, C 1s and Ru 3d, Fe 2p, K 2p, and P 2p, respectively, which signify the presence of O, C, Ti, Fe, Ru, K, and P elements within the composite material. To further scrutinize these characteristic elements, high-resolution XPS spectra were acquired (Fig. 2b–g). The high-resolution O 1s spectrum (Fig. 2b) was deconvoluted into three distinct peaks. The peak located at 530.08 eV is ascribed to lattice oxygen,[40] which is associated with O–Ti bonds in Ru-TiO_2, Ru–O bonds, and O–Fe bonds in Fe_3O_4. The binding energy of lattice oxygen in Ru-TiO_2/PC/Fe_3O_4 (530.08 eV) exhibits a marked blue shift when compared to Ru-TiO_2/PC (529.68 eV), suggesting an enhanced interfacial interaction between TiO_2 and Fe_3O_4, which may

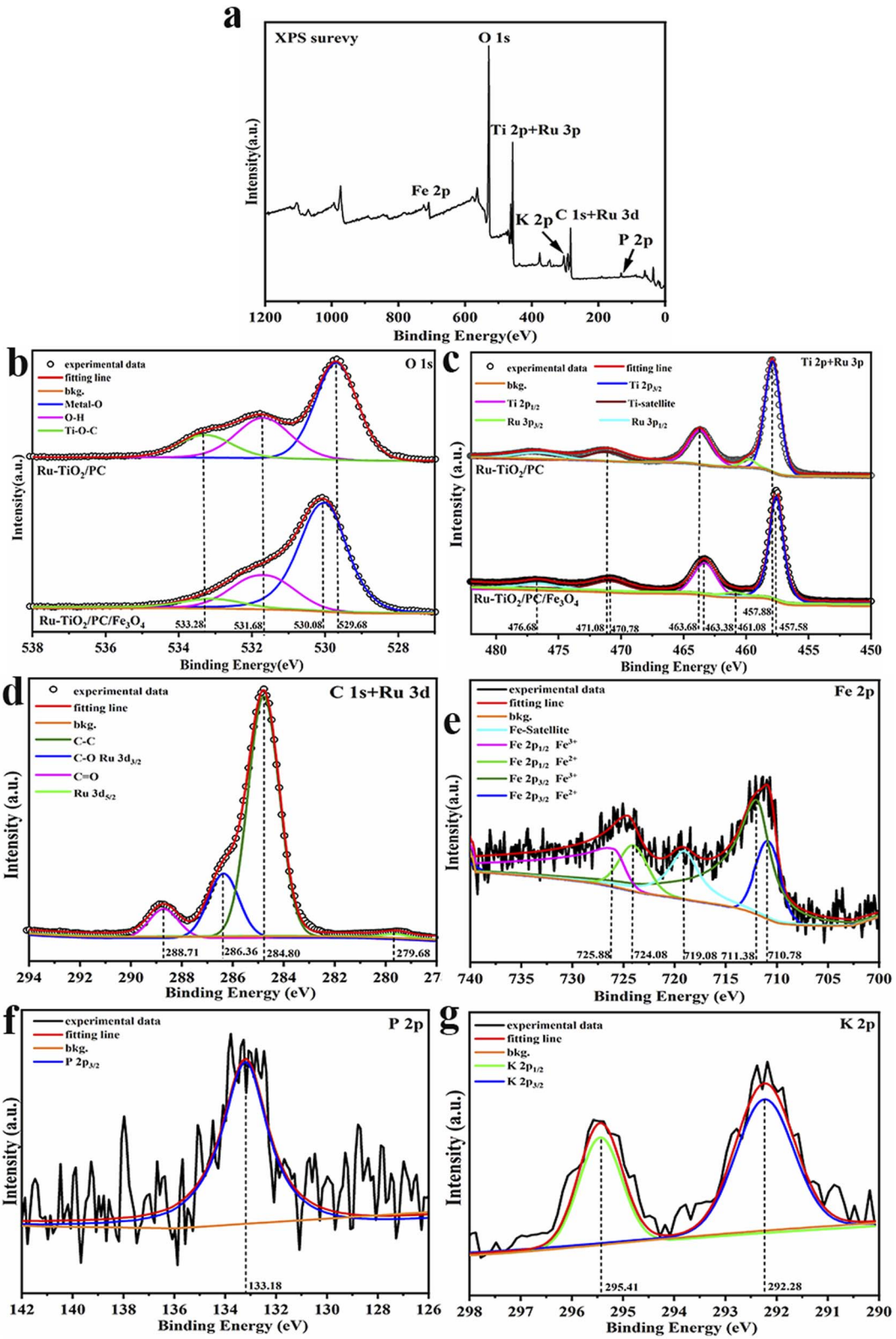

Fig. 2 XPS spectra of Ru-TiO_2/PC/Fe_3O_4 sample: (a) full survey spectrum; (b) combined peaks of Ti 2p and Ru 3p; (c) O 1s spectrum; (d) Fe 2p spectrum; (e) combined peaks of C 1s and Ru 3d; (f) P 2p spectrum; (g) K 2p spectrum.

indicate the formation of a heterojunction[40,41]. The peaks at 533.28 eV and 531.68 eV are assigned to O–H bonds and Ti–O–C bonds, respectively.[42,43] The presence of O–H bonds is advantageous for the generation of ·OH radicals, thereby enhancing catalytic activity, whereas the Ti–O–C bonds imply the incorporation of a minor amount of C atoms into the TiO_2

Table 2 XPS binding energy and atomic percentage evaluation results for Ru-TiO_2/PC/Fe_3O_4 samples

Element	BE/eV	Group	At. %	
Ti 2p	457.92	Ti–O	10.22	14.19
	463.61	Ti–O	3.97	
Ru 3p	461.08	Ru^{4+}	0.19	0.72
	476.68	Ru^{4+}	0.53	
O 1s	530.29	Ti–O/Fe–O/Ru-O	29.52	45.92
	531.98	O–H	11.65	
	533.40	C–O/P–O/O–H	4.75	
C 1s	284.80	C–C/H	20.37	34.94
	286.36	C–O	10.29	
	288.71	C–O–Ti, C=O	4.28	
Ru 3d	279.61	Ru^{4+}	0.43	0.43
P 2p	133.18	P–O	0.48	0.48
K 2p	292.28	K^+	0.24	0.41
Fe 2p	295.41	K^+	0.17	2.91
	710.78	Fe^{2+}	0.52	
	711.38	Fe^{3+}	1.37	
	724.08	Fe^{2+}	0.43	
	725.88	Fe^{3+}	0.59	

lattice during calcination.[44] The high-resolution Ti 2p and Ru 3p spectrum (Fig. 2c) was resolved into five peaks. The characteristic peaks at 469.98 eV, 463.38 eV, and 457.58 eV correspond to the satellite peak of Ti, Ti $2p_{1/2}$, and Ti $2p_{3/2}$, respectively, which are indicative of Ti^{4+} species.[45] These peaks, when compared to Ru-TiO_2/PC, exhibit a red shift of approximately 0.3 eV, suggesting a reduction in the binding energy of TiO_2 as a consequence of the heterojunction between Fe_3O_4 and TiO_2.[46] Additionally, the peaks at 476.68 eV and 461.08 eV are attributed to Ru $3p_{1/2}$ and Ru $3p_{3/2}$ characteristic peaks, respectively.[47] The high-resolution C 1s + Ru 3d spectrum (Fig. 2d) was deconvoluted into four distinct peaks. The peaks at 288.71 eV and 284.80 eV correspond to C=O and C–C bonds, respectively.[48] The peak at 286.36 eV represents an overlap of C–O bonds and Ru $3d_{3/2}$, while the peak at 279.68 eV is assigned to Ru $3d_{5/2}$.[49] The high-resolution Fe 2p spectrum (Fig. 2e) reveals five peaks. The characteristic peak at 719.08 eV is identified as the satellite peak of Fe. The peaks located at 725.88 eV, 724.08 eV, 711.38 eV, and 710.78 eV correspond to Fe $2p_{1/2}$ (Fe^{3+}), Fe $2p_{1/2}$ (Fe^{2+}), Fe $2p_{3/2}$ (Fe^{3+}), and Fe $2p_{3/2}$ (Fe^{2+}) characteristic peaks, respectively.[50] The atomic ratio of Fe^{3+} to Fe^{2+} is estimated to be approximately 2 : 1, which is consistent with the properties of Fe_3O_4.[51] The high-resolution P 2p and K 2p spectra (Fig. 2f and g) confirm the presence of P and K elements.[52,53] Grapefruit peel, as a biomass source, naturally contains minerals such as phosphorus and potassium, which may exist in the form of inorganic salts or organic compounds. During the catalyst preparation process, these elements might be retained and incorporated into the final material.

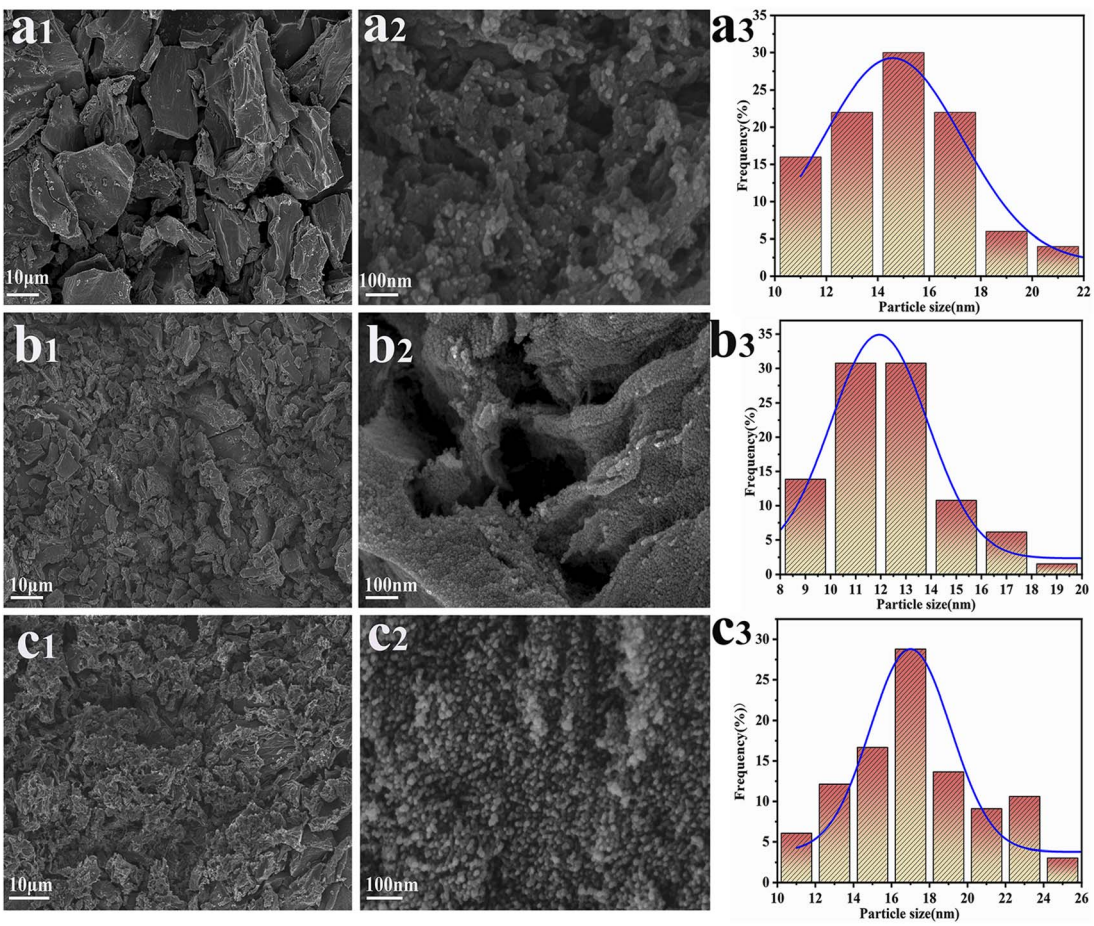

Fig. 3 SEM images and particle size distribution diagrams of Fe_3O_4/PC (a_1–a_3), Ru-TiO_2/PC (b_1–b_3), and Ru-TiO_2/PC/Fe_3O_4 (c_1–c_3) samples.

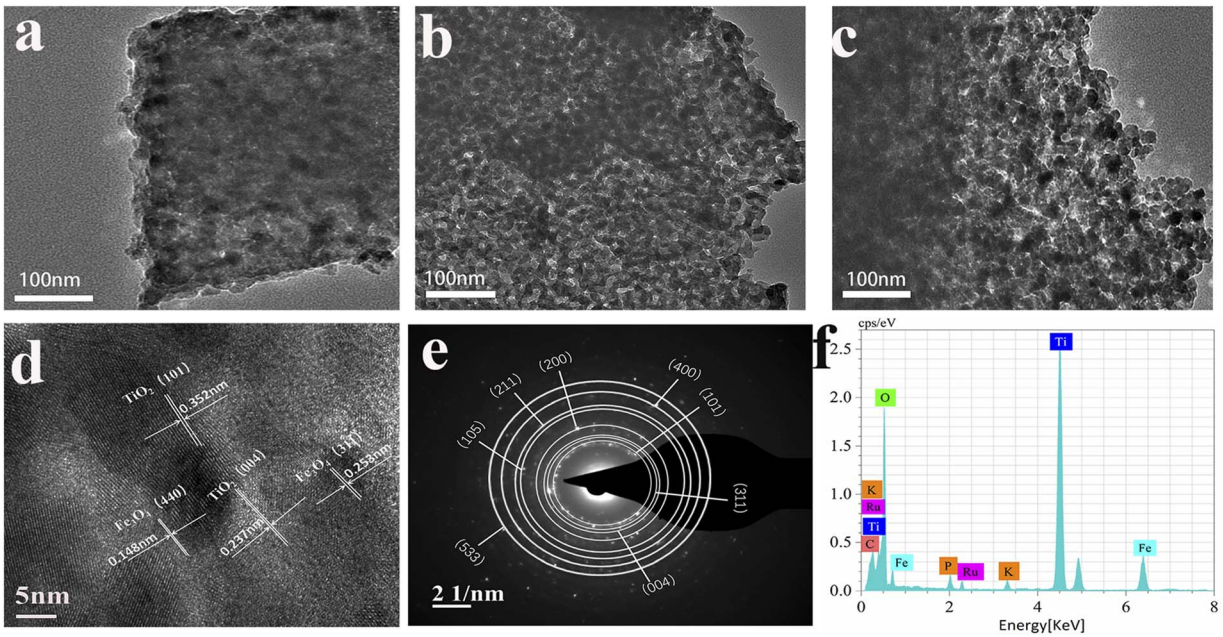

Fig. 4 (a) Fe_3O_4/PC, (b) Ru-TiO_2/PC, (c) Ru-TiO_2/PC/Fe_3O_4 transmission electron microscopy images of three samples, (d) HRTEM image of the Ru-TiO_2/PC/Fe_3O_4 sample, (e) SAED pattern and (f) EDS spectrum of Ru-TiO_2/PC/Fe_3O_4 sample.

Table 2 provides an overview of the XPS binding energy and atomic percentage evaluation results for the Ru-TiO_2/PC/Fe_3O_4 sample. The findings from the XPS analysis suggest that the synthesis of the Ru-TiO_2/PC/Fe_3O_4 composite with heteroatoms of P and K, was successfully achieved.

3.3 Morphological analysis of Ru-TiO_2/PC/Fe_3O_4

To explore the morphological structure of the samples, field emission scanning electron microscopy (SEM) was utilized to characterize Fe_3O_4/PC, Ru-TiO_2/PC, and Ru-TiO_2/PC/Fe_3O_4. The corresponding results are depicted in Fig. 3. Fig. $3a_1$–a_3 provide the SEM images and particle size distribution of the Fe_3O_4/PC sample. It can be observed that the Fe_3O_4/PC sample effectively mirrors the morphological structure of the GP powder (Fig. $3a_1$). At higher magnification (Fig. $3a_2$), the wrinkled and porous architecture of the GP biochar is distinctly visible, with spherical Fe_3O_4 nanoparticles uniformly distributed across its surface, exhibiting no signs of agglomeration. The particle size

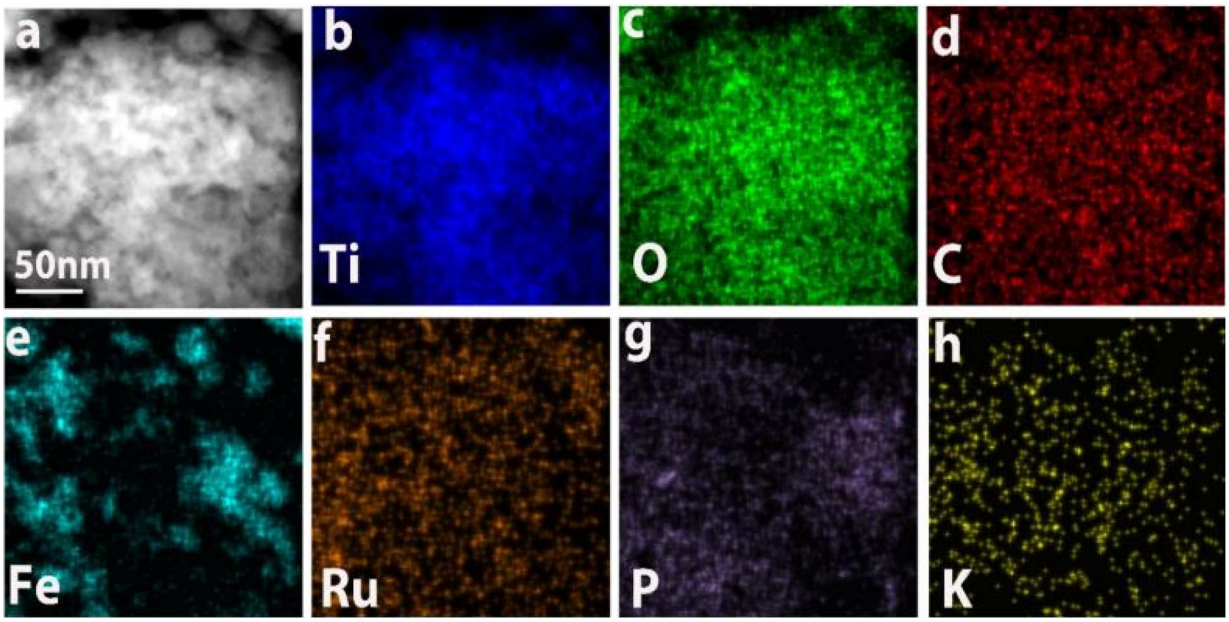

Fig. 5 TEM image (a) and the corresponding elemental mapping images of (b) Ti, (c) O, (d) C, (e) Fe, (f) Ru, (g) P, and (h) K for the Ru-TiO_2/PC/Fe_3O_4 sample.

distribution graph (Fig. 3a$_3$) reveals that the diameter of the Fe_3O_4 particles is predominantly within the range of 10–20 nm. Fig. 3b$_1$–b$_3$ display SEM images of the Ru-TiO_2/PC sample at various magnifications, alongside its particle size distribution. It is evident that Ru-TiO_2/PC primarily consists of spherical nanoparticles with diameters ranging from 10–14 nm, which are uniformly aligned along the GP fibers, resulting in a well-defined porous structure. Fig. 3c$_1$–c$_3$ showcase SEM images of the Ru-TiO_2/PC/Fe_3O_4 sample at different magnifications. The sample exhibits pronounced porosity and a layered structure, with its surface covered by nanoparticles. Upon further magnification (Fig. 3c$_2$), it is revealed that spherical nanoparticles are evenly dispersed on the biochar, with porous structures evident in the composite material. The particle size distribution graph (Fig. 3c$_3$) indicates that the particle sizes within the composite material are primarily concentrated between 10–20 nm.

To further examine the microstructure of the samples, field emission transmission electron microscopy was utilized to characterize the Fe_3O_4/PC, Ru-TiO_2/PC, and Ru-TiO_2/PC/Fe_3O_4 samples, as depicted in Fig. 4. In Fig. 4a, it is evident that quasi-spherical Fe_3O_4 nanoparticles are uniformly distributed on the biochar within the Fe_3O_4/PC sample, with no evidence of agglomeration and particle diameters ranging from 10 to 20 nm. Fig. 4b illustrates that the Ru-TiO_2/PC sample is composed of nanoparticles integrated with thin carbon layers, where quasi-spherical Ru-TiO_2 nanoparticles are systematically aligned along the biochar fibers, with particle diameters between 10 and 14 nm. Fig. 4c demonstrates that both Fe_3O_4 and Ru-TiO_2 nanoparticles are uniformly dispersed on the GP biochar in the Ru-TiO_2/PC/Fe_3O_4 sample, with particle sizes approximately between 10 and 20 nm, which aligns with the SEM observations. Fig. 4d presents the high-resolution transmission electron microscopy (HRTEM) image of the Ru-TiO_2/PC/Fe_3O_4 sample, revealing four distinct lattice fringes. The lattice spacings of 0.253 nm and 0.148 nm are associated with the (311) and (440) crystal planes of Fe_3O_4,[39] while the spacings of 0.352 nm and 0.237 nm correspond to the (101) and (004) crystal planes of TiO_2,[35] corroborating the XRD results. Due to the similar ionic radii of Ru^{4+} and Ti^{4+}, and the minimal doping concentration of Ru, the incorporation of Ru did not significantly alter the lattice structure of TiO_2.[49] Fig. 4e displays the selected area electron diffraction (SAED) pattern of the Ru-TiO_2/PC/Fe_3O_4 sample, showing diffraction rings corresponding to the (101) and (004) crystal planes of TiO_2 and the (311) crystal plane of Fe_3O_4, indicative of a polycrystalline structure. Fig. 4f presents the energy dispersive X-ray spectroscopy (EDS) spectrum of the Ru-TiO_2/PC/Fe_3O_4 sample, which further verifies the presence of Ti, O, C, Fe, Ru, P, K, and other elements in the sample.

Fig. 5 illustrates the transmission electron microscopy (TEM) elemental mapping of the Ru-TiO_2/PC/Fe_3O_4 sample. The mapping delineates the distribution of Ti, O, C, Fe, Ru, P, and K elements. Ti, O, and C are observed to be extensively and uniformly dispersed, maintaining shapes consistent with the TEM mapping of the sample. Fe is primarily present in the form of spots and clusters, indicative of an uneven distribution of iron.

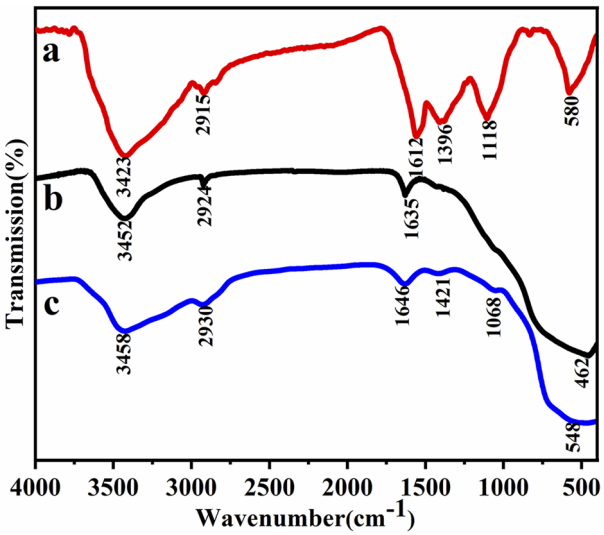

Fig. 6 The FTIR spectrum of (a) Fe_3O_4/PC, (b) Ru-TiO_2/PC, and (c) Ru-TiO_2/PC/Fe_3O_4.

Ru is sparsely but evenly distributed, exhibiting a shape akin to Ti, which suggests uniform doping of Ru into TiO_2. P and K are distributed as uniform small dots, indicating that despite their low concentrations, their distribution is homogeneous, likely originating from the biochar-based material. Correlating these findings with the results from XRD, Raman, and XPS analyses, it can be concluded that the Ru-TiO_2/PC/Fe_3O_4 composite material, comprising Ru-doped TiO_2, GP biochar, and Fe_3O_4 with P and K elements, has been successfully synthesized.

3.4 Mechanism of formation of the Ru-TiO_2/PC/Fe_3O_4 composite

To elucidate the formation mechanism of the Ru-TiO_2/PC/Fe_3O_4 composite, Fourier-transform infrared (FTIR) spectroscopy was performed on Fe_3O_4/PC, Ru-TiO_2/PC, and Ru-TiO_2/PC/Fe_3O_4. The results are presented in Fig. 6.

As depicted in the figure, three samples exhibit a prominent and broad peak around 3400 cm^{-1}, which is attributed to the

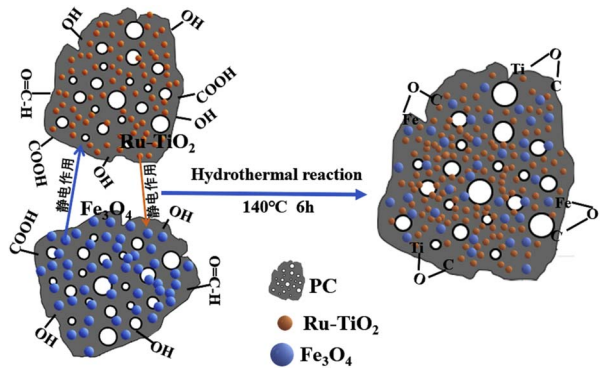

Fig. 7 Schematic diagram of the formation process of the Ru-TiO_2/PC/Fe_3O_4 composite.

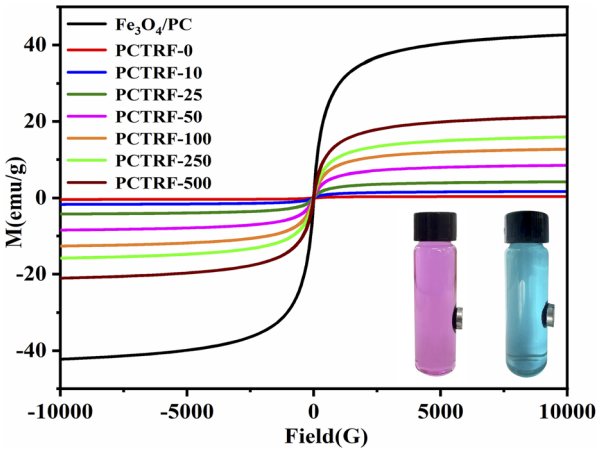

Fig. 8 Magnetic hysteresis loops of Fe_3O_4/PC and PCTRF-x (x = 0, 10, 25, 50, 100, 250, 500) samples.

stretching vibrations of –OH groups.[54] Furthermore, distinct stretching vibration peaks corresponding to C–H bonds, C=O, and C–O–C are observed near 2900 cm^{-1} and 1600 cm^{-1}. These findings indicate the presence of abundant functional groups, such as hydroxyl and carboxyl groups, in the samples.[55] In the FTIR spectrum of Fe_3O_4/PC (Fig. 6a), the peaks observed at 1396 cm^{-1} and 1118 cm^{-1} are attributed to the stretching vibrations of C–H and C–O, respectively. Additionally, the characteristic peak located around 580 cm^{-1} corresponds to the Fe–O bond.[56] Combined with the XRD analysis, these results further confirm the presence of Fe_3O_4. In the FTIR spectrum of the Ru-TiO_2/PC sample (Fig. 6b), a prominent and broad peak at 462 cm^{-1} is observed, corresponding to Ti–O–Ti bonds, which are characteristic of the TiO_2 structure.[57] In the FTIR spectrum of Ru-TiO_2/PC/Fe_3O_4 (Fig. 6c), alongside the characteristic peaks of biochar, additional peaks corresponding to Ti–O, Fe–O, and Ti–O–C bonds are observed. These results not only confirm the successful synthesis of the Ru-TiO_2/PC/Fe_3O_4 composite but also highlight its intricate chemical structure.

Based on the comprehensive analysis results from XRD, XPS, Raman, SEM, and FTIR, a formation mechanism model for the Ru-TiO_2/PC/Fe_3O_4 composite material was proposed, as illustrated in Fig. 7. The surface of biochar is abundant in functional groups, including –OH and –COOH, which interact with TiO_2 and Fe_3O_4 nanoparticles through hydrogen bonding and van der Waals forces. These interactions strengthen the adhesion between the nanoparticles and the biochar, contributing to the composite's structural stability. Furthermore, the –OH and –COOH groups on the biochar surface confer a negative charge, whereas the surfaces of the metal oxide particles exhibit

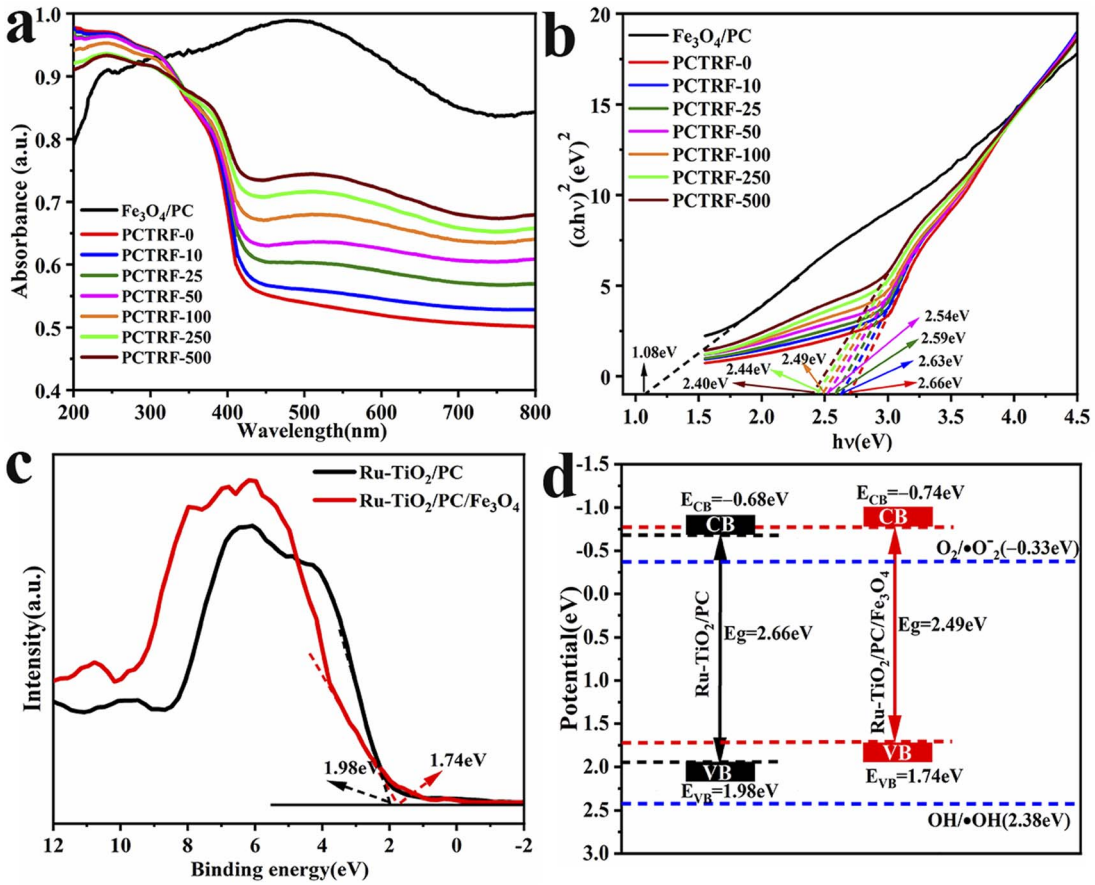

Fig. 9 (a) UV-vis DRS spectra of Fe_3O_4/PC and Ru-TiO_2/PC/Fe_3O_4 series samples, (b) Tauc plot curves, (c) VB-XPS spectra of Ru-TiO_2/PC and Ru-TiO_2/PC/Fe_3O_4 samples, and (d) band gap structure.

a positive charge. This electrostatic interaction facilitates the binding of biochar in Ru-TiO_2/PC with Fe_3O_4 particles, as well as the interaction of biochar in Fe_3O_4/PC with TiO_2 particles, leading to the formation of primary composite structures. During the hydrothermal reaction, suitable temperature and pressure conditions promote coordination and condensation reactions between the carboxyl and hydroxyl groups on the biochar surface and the TiO_2 and Fe_3O_4 nanoparticles. These interactions result in the formation of stable oxygen bridges (*e.g.*, Ti–O–C and Fe–O–C), which significantly enhance the structural stability of the composite material. This effective microscopic bonding between the metal oxide particles and the biochar ultimately leads to the formation of a porous Ru-TiO_2/PC/Fe_3O_4 composite.

3.5 Magnetic properties of Ru-TiO_2/PC/Fe_3O_4

The magnetic hysteresis loops of Fe_3O_4/PC and the Ru-TiO_2/PC/Fe_3O_4 series samples were evaluated through the application of a vibrating sample magnetometer (VSM), with the results illustrated in Fig. 8.

As depicted in the figure, all samples are characterized by "S"-shaped magnetization curves. The saturation magnetization (M_s) of Fe_3O_4/PC is recorded at 43.86 emu g^{-1}, whereas the M_s values of the Ru-TiO_2/PC/Fe_3O_4 series samples are observed to be lower than this benchmark, progressively increasing as the Fe_3O_4/PC content rises. Notably, the M_s of the PCTRF-0 sample approximates zero, signifying non-magnetic characteristics. In contrast, the M_s of the PCTRF-500 sample is measured at 22.01 emu g^{-1}, which indicates pronounced magnetic properties. The inset in Fig. 8 demonstrates the separation effect of the PCTRF-100 sample in RhB and MB solutions after exposure to an external magnetic field for 5 min. This observation confirms that the Ru-TiO_2/PC/Fe_3O_4 sample can be effectively segregated from the solution under the influence of an external magnetic field, thereby enhancing its recyclability.

3.6 Photoelectric performance of Ru-TiO_2/PC/Fe_3O_4

To explore the light absorption characteristics of the materials and determine their band gap energies, UV-visible diffuse reflectance spectroscopy (UV-vis DRS) was employed on the Fe_3O_4/PC and Ru-TiO_2/PC/Fe_3O_4 series samples, with the findings depicted in Fig. 9a. It can be seen from the figure that the Fe_3O_4/PC sample demonstrated a distinct absorption peak around 480 nm, which indicates strong absorption within the visible light spectrum. With the increasing content of Fe_3O_4/PC, the Ru-TiO_2/PC/Fe_3O_4 series samples progressively exhibited the characteristic absorption peak of Fe_3O_4, and their light absorption intensity in the visible region was significantly augmented.

The Kubelka–Munk formula and Tauc plots method were combined to plot the Tauc plot curve,[58,59] as depicted in Fig. 9b. The band gap energy (E_g) was determined by extrapolating the linear segment to its intersection with the *x*-axis. The calculated E_g for Fe_3O_4/PC was approximately 1.08 eV, while that for Ru-TiO_2/PC was around 2.66 eV. For the Ru-TiO_2/PC/Fe_3O_4 series samples, the band gap energy E_g decreased from 2.63 eV to 2.40 eV, suggesting that Ru-TiO_2/PC/Fe_3O_4 exhibits a narrower band gap, facilitating the easier excitation of electrons.

Valence band X-ray photoelectron spectroscopy (VB-XPS) tests were performed on Ru-TiO_2/PC (PCTRF-0) and Ru-TiO_2/PC/Fe_3O_4 (PCTRF-100) samples. The valence band potentials (E_{VB}) were estimated at 1.98 eV and 1.74 eV, respectively, using the linear extrapolation method (Fig. 9c). Utilizing the formula $E_{CB} = E_{VB} - E_g$,[60] the conduction band potentials (E_{CB}) for the two samples were calculated as −0.68 eV and −0.74 eV, respectively. From these data, the band structure diagram of the samples was constructed (Fig. 9d). As illustrated in the figure, both the E_{VB} and E_{CB} of Ru-TiO_2/PC/Fe_3O_4 exhibit a shift towards the negative direction compared to Ru-TiO_2/PC. This shift indicates that the Ru-TiO_2/PC/Fe_3O_4 composite material possesses a higher electron transfer efficiency, facilitating the effective separation of photogenerated electron–hole pairs and thereby enhancing its photocatalytic performance.[61] Therefore, the Ru-TiO_2/PC/Fe_3O_4 composite material shows considerable potential for applications in photocatalysis.

To assess the photogenerated electron–hole separation and transport efficiency of the samples, photocurrent measurements, electrochemical impedance spectroscopy (EIS), and photoluminescence (PL) tests were performed on Fe_3O_4/PC and Ru-TiO_2/PC/Fe_3O_4 series samples. The results are presented in Fig. 10. The photocurrent–time response curves (Fig. 10a) reveal that all samples display rapid and stable responses to the light source, thereby demonstrating their capability to generate photoinduced carriers. Notably, the PCTRF-100 sample exhibits the highest photocurrent, which signifies superior carrier separation and transport efficiency. The EIS data (Fig. 10b) indicate that the Ru-TiO_2/PC/Fe_3O_4 sample possesses the lowest impedance, implying an optimal carrier transport rate. The PL spectra (Fig. 10c) indicate that the Fe_3O_4/PC sample shows the highest PL peak intensity, whereas the PCTRF-100 sample displays the lowest PL peak intensity. A reduced PL peak intensity suggests a lower electron–hole recombination efficiency,[62] indicating that the PCTRF-100 sample achieves the lowest photogenerated electron–hole recombination rate. In conclusion, the PCTRF-100 sample demonstrates superior carrier separation and transport efficiency, as well as the lowest electron–hole recombination rate, underscoring its potential as a highly efficient photocatalyst.

3.7 Photocatalytic performance of Ru-TiO_2/PC/Fe_3O_4

The photocatalytic degradation efficiency of the Ru-TiO_2/PC/Fe_3O_4 composite material for RhB, MB, MO, and actual IDW under simulated solar light was assessed, with the corresponding results presented in Fig. 11. Fig. 11a–c illustrate that, in the absence of photocatalysts, the degradation efficiencies of RhB, MO, and MB remain extremely low, suggesting that these dyes are relatively stable under simulated solar light, making them suitable as target pollutants for photodegradation experiments. During the dark adsorption phase, the Fe_3O_4/PC sample exhibits adsorption rates of 50.78%, 54.46%, and 24.78% for RhB, MB, and MO, respectively, which significantly exceed those of the Ru-TiO_2/PC/Fe_3O_4 series samples. This enhanced performance can be attributed to its higher biochar content and larger specific surface area. For the Ru-TiO_2/PC/Fe_3O_4 series

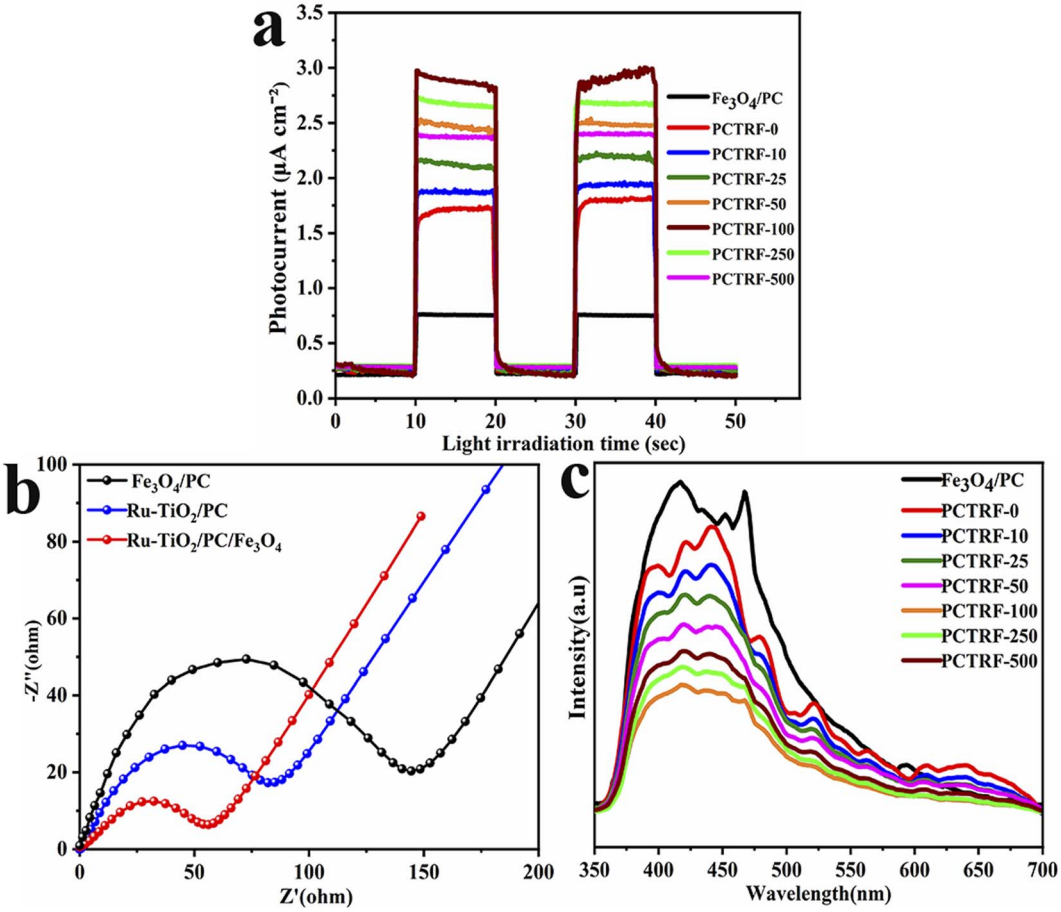

Fig. 10 (a) Time-dependent photocurrent response curves; (b) EIS plots; and (c) PL spectra of Fe_3O_4/PC and Ru-TiO_2/PC/Fe_3O_4 series samples.

samples, the adsorption capacity for RhB, MB, and MO initially increases and subsequently decreases as the Fe_3O_4/PC content rises, with the PCTRF-100 sample demonstrating the most effective adsorption performance. During the photocatalytic degradation phase, Fe_3O_4/PC shows low degradation efficiency for RhB, MB, and MO, indicating inadequate photocatalytic activity. Under simulated solar light, the Ru-TiO_2/PC/Fe_3O_4 series samples rapidly enhance the degradation efficiencies of RhB and MB within the first 30 min, reaching equilibrium after 60 min. For MO, a rapid decrease in degradation efficiency is observed within 80 min, followed by equilibrium after 120 min. As the Fe_3O_4/PC content increases, the photocatalytic performance of the composite catalyst initially improves and then declines. Among the samples, PCTRF-100 exhibits the most superior photocatalytic performance, achieving degradation rates of 99.4% and 99.8% for RhB and MB within 60 min, respectively, and 98.04% for MO within 120 min. These findings clearly indicate that an optimal mass ratio of Fe_3O_4/PC to Ru-TiO_2/PC in the composite material is essential for maximizing photocatalytic performance. However, an excessive amount of Fe_3O_4 can cover the active sites of TiO_2, thereby diminishing its surface activity and light transmittance, which in turn negatively impacts its photocatalytic efficiency.

To assess the degradation effectiveness of the Ru-TiO_2/PC/Fe_3O_4 composite catalyst on actual IDW, the best-performing PCTRF-100 sample was selected for experimentation. The IDW used in the experiment was obtained from a dyeing factory in Shantou City, Guangdong Province, and was characterized by an initial pH of approximately 8.0 and a chemical oxygen demand (COD) of about 1540 mg L^{-1}. Due to the complex composition and high content of solid suspended particles in the dye wastewater, pretreatment was required prior to the experiment, involving multiple filtrations and high-speed centrifugation to eliminate solid suspended particles. Following pretreatment, 5 mL of the supernatant was diluted to 100 mL, and 50 mg of the PCTRF-100 sample was added. The photocatalytic experiment was carried out according to the procedure described in Section 2.3, with absorbance measured at a wavelength of 240 nm. The C/C_0–t relationship curve was plotted, as depicted in Fig. 11d. The results showed that under simulated solar light, the PCTRF-100 sample exhibited photocatalytic activity toward actual IDW, achieving a degradation efficiency of 46.82% after 300 min of irradiation. This efficiency was significantly lower than that observed for single dye solutions, reflecting the complexity of actual IDW. Although the photocatalytic degradation effect of the PCTRF-100 sample on actual IDW did not fully meet expectations, it was able to reduce

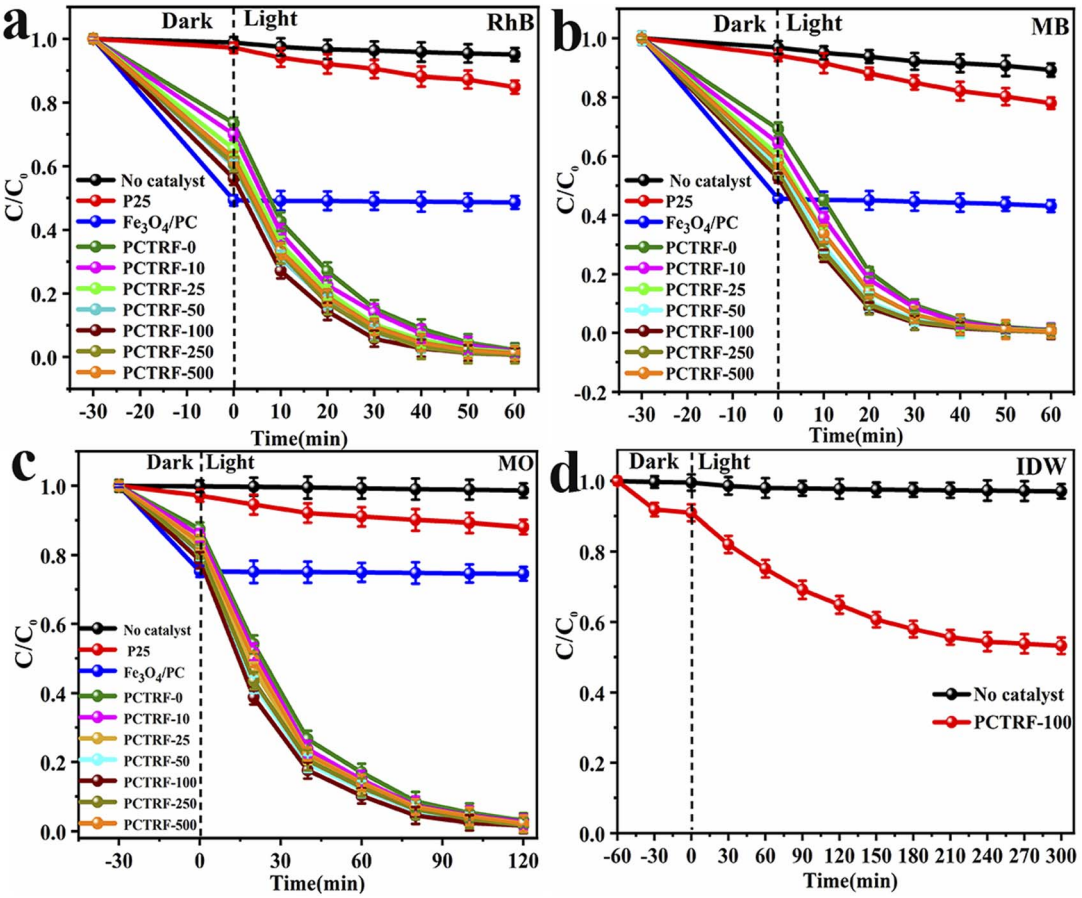

Fig. 11 C/C_0–t relationship curves with error bars for photocatalytic degradation of different organic pollutants by P25, Fe_3O_4/PC, and Ru-TiO_2/PC/Fe_3O_4 series samples: (a) RhB, (b) MB, (c) MO; (d) C/C_0–t relationship curve for photocatalytic degradation of IDW by PCTRF-100 sample.

the COD value of IDW from 1540 mg L^{-1} to 784 mg L^{-1}, demonstrating its potential value in treating actual IDW.

Furthermore, kinetic analysis was performed on the photocatalytic degradation processes of RhB, MB, MO, and IDW by the Ru-TiO_2/PC/Fe_3O_4 series samples, with the results presented in Fig. 12 and Table 3. As depicted in Fig. 12a–c, the photocatalytic degradation of RhB, MB, and MO by the Ru-TiO_2/PC/Fe_3O_4 series samples conforms well to a linear first-order kinetic model, with R^2 values exceeding 0.99, which indicates a high degree of correlation. The data in Table 3 show that the rate constants (k) for the P25 and Fe_3O_4/PC samples are relatively low. The k values of the Ru-TiO_2/PC/Fe_3O_4 series samples initially increase and then decrease as the Fe_3O_4/PC content is increased. Among these samples, the PCTRF-100 sample exhibits the highest k values, with k_{RhB}, k_{MB}, and k_{MO} measured at 0.07667 min^{-1}, 0.08671 min^{-1}, and 0.03458 min^{-1}, respectively, confirming its superior photocatalytic performance. Due to its complexity, a non-linear kinetic model was employed to fit the actual IDW. The model equation is given by $A_t = Xe^{-kt} + E$, where A_t represents the absorbance of residual pollutants, X is the reaction amplitude, k denotes the rate constant, and E is the reaction endpoint.[63] After fitting, an R^2 value of 0.998 was obtained, indicating that the process of the PCTRF-100 sample in treating actual IDW aligns well with the non-linear least squares kinetic model (Fig. 12d). The rate constant was determined to be 0.001673 min^{-1}, demonstrating its effectiveness in treating actual dye wastewater.

The PCTRF-100 sample, which exhibited the highest photocatalytic performance, was compared with other magnetic catalysts reported in the literature, as summarized in Table 4. It can be seen that PCTRF-100 demonstrated superior degradation efficiency for RhB, MB, and MO under simulated solar light when compared to previously reported magnetic composite catalysts. To date, there have been no reports in the literature on the use of magnetic composite photocatalysts for the degradation of actual dye wastewater. However, the Ru-TiO_2/PC/Fe_3O_4 composite catalyst investigated in this study also exhibited photocatalytic activity in treating actual IDW.

3.8 Recyclability of Ru-TiO_2/PC/Fe_3O_4

The recyclability and cyclic stability of catalysts are essential factors for their practical application and commercial viability. Therefore, the Ru-TiO_2/PC/Fe_3O_4 sample with the highest photocatalytic performance was selected for five cycles of degradation experiments on MB solution and actual dye wastewater to assess its cyclic stability. In these experiments, after each reaction, the catalyst was separated and recovered using an external magnetic field, then washed, dried, and reused. Each

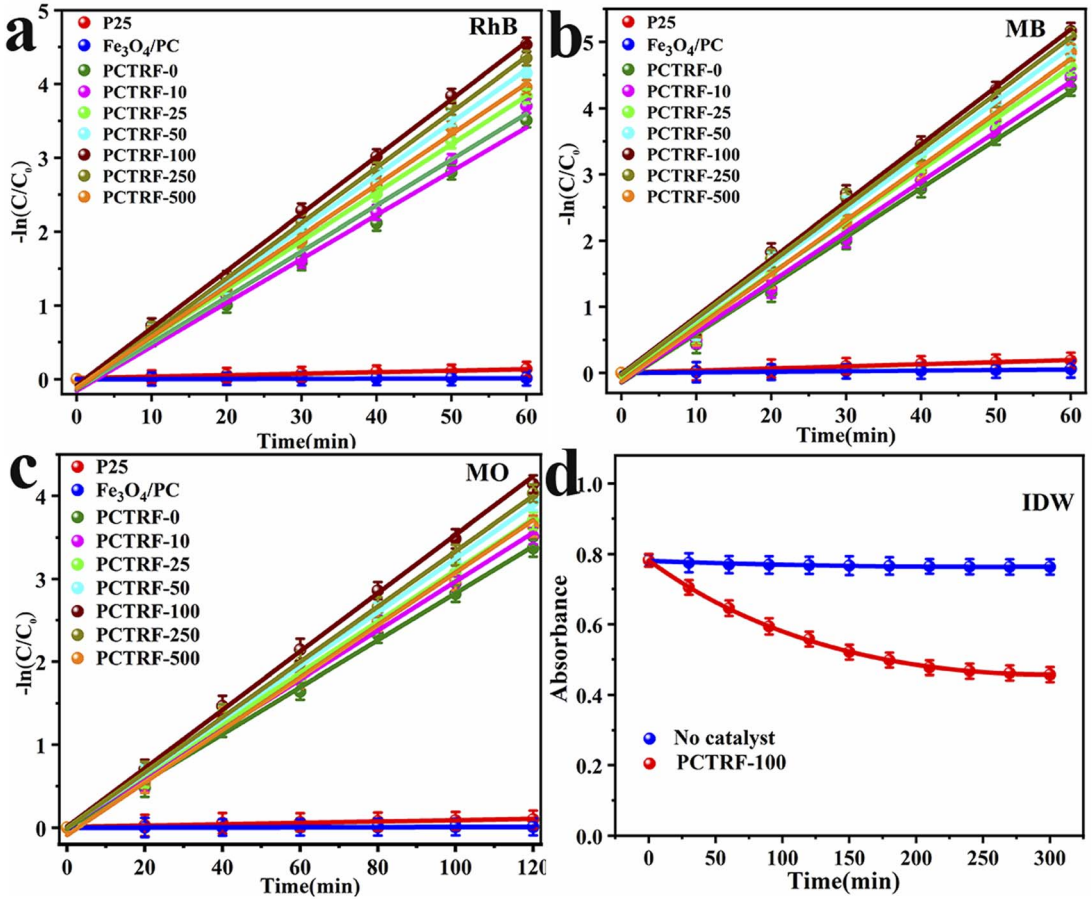

Fig. 12 Reaction kinetics curves with error bars for the photocatalytic degradation of: (a) RhB, (b) MB, and (c) MO using P25, Fe_3O_4/PC, and Ru-TiO_2/PC/Fe_3O_4 series samples. (d) Non-linear kinetics curve for the photocatalytic degradation of actual dye wastewater using the PCTRF-100 sample.

cycle was performed under identical conditions, and the recovery rate and degradation rate were calculated. The results are depicted in Fig. 13.

Fig. 13a and b indicate that after five cycles, Ru-TiO_2/PC/Fe_3O_4 maintained good recovery and photocatalytic activity for both MB solution and actual IDW. The recovery rate remained above 93%, while the degradation rate of MB reached 91.38%, with only a slight decrease observed in the degradation rate for IDW. ANOVA and Tukey's tests confirmed significant differences in degradation rates across cycles ($p < 0.05$). This decline is likely due to dye molecules blocking or damaging the catalyst's porous structure, reducing active sites. Fig. 13c illustrates that the recovery rate of Ru-TiO_2/PC/Fe_3O_4 is significantly higher than that of other catalysts, being 18.62%, 17.62%, and 20.76% higher than Ru-TiO_2/PC, TiO_2/PC, and P25, respectively. Fig. 13d presents a comparison of XPS spectra for samples before and after cyclic reactions. Although the intensity of some characteristic peaks weakened after five rounds of photodegradation, no new diffraction peaks were observed, suggesting that while some active sites of the catalyst may have been partially passivated, its

Table 3 Kinetic rate constants of P25, Fe_3O_4/PC, and Ru-TiO_2/PC/Fe_3O_4 series samples

Samples	k_{RhB} (min^{-1})	R_{RhB}^2	k_{MB} (min^{-1})	R_{MB}^2	k_{MO} (min^{-1})	R_{MO}^2	k_{IDW} (min^{-1})	R_{IDW}^2
P25	0.00215	0.9872	0.00320	0.9903	0.00077	0.9885	—	—
Fe_3O_4/PC	0.00022	0.9819	0.00089	0.9837	0.000076	0.9820	—	—
PCTRF-0	0.05763	0.9949	0.07420	0.9950	0.02843	0.9980	—	—
PCTRF-10	0.06062	0.9947	0.07644	0.9958	0.02954	0.9982	—	—
PCTRF-25	0.06454	0.9989	0.07853	0.9978	0.03081	0.9993	—	—
PCTRF-50	0.07046	0.9986	0.08266	0.9977	0.03241	0.9992	—	—
PCTRF-100	0.07667	0.9987	0.08671	0.9970	0.03458	0.9992	0.006515	0.9982
PCTRF-250	0.07358	0.9983	0.08500	0.9972	0.03327	0.9997	—	—
PCTRF-500	0.06735	0.9979	0.08199	0.9963	0.03029	0.9974	—	—

Table 4 Comparison of catalytic performance between Ru-TiO_2/PC/Fe_3O_4 and other reported magnetic composite photocatalysts

Photocatalyst	Dosage (mg/100 mL)	Light source	Irradiation time (min)	Pollutant (conc.)	Removal efficiency (%)	Ref.
Fe_3O_4@Ru-TiO_2	30	300 W Xe lamp	120	MB (15 mg L^{-1})	70.20	2
TiO_2/SiO_2@Fe_3O_4	100	1.5 kW Xe lamp	60	Ketamine (76 μg L^{-1})	100	64
C–TiO_2@Fe_3O_4/AC	100	300 W Xe lamp	30	Congo red (100 mg L^{-1})	92.92	65
Fe_3O_4/TiO_2	100	Direct sunlight	40	MB (5 ppm)	97.00	28
g-C_3N_4/Fe_3O_4/TiO_2	30	500 W Xe lamp	120	MB (10 mg L^{-1})	98.10	66
Fe_3O_4–TiO_2	100	500 W Xe lamp	40	RhB (5 mg L^{-1})	99.20	67
Fe_3O_4/C/TiO_2	100	500 W Xe lamp	120	Phenol (10 mg L^{-1})	82.46	68
C–TiO_2/Fe_3O_4	20	Natural sunlight	150	MO (5 mg L^{-1})	99.68	69
Ru-TiO_2/PC/Fe_3O_4	50	600 W Xe lamp	60	RhB (10 mg L^{-1})	99.21	This work
Ru-TiO_2/PC/Fe_3O_4	50	600 W Xe lamp	60	MB (10 mg L^{-1})	99.70	This work
Ru-TiO_2/PC/Fe_3O_4	50	600 W Xe lamp	120	MO (10 mg L^{-1})	98.31	This work
Ru-TiO_2/PC/Fe_3O_4	50	600 W Xe lamp	300	Industrial dye wastewater	46.81	This work

chemical composition remained unchanged. This stability could be attributed to the advantages conferred by the composite structure of Ru-TiO_2/PC and Fe_3O_4/PC.

3.9 Photocatalytic mechanism of Ru-TiO_2/PC/Fe_3O_4 composite

To elucidate the mechanism underlying the photocatalytic degradation of dye wastewater by Ru-TiO_2/PC/Fe_3O_4, electron paramagnetic resonance (EPR) tests were conducted to analyze the active free radicals generated during the photocatalytic reaction. Under xenon lamp irradiation, DMPO was utilized as a spin-trapping agent to capture ·OH and $\cdot O_2^-$, while TEMPO was employed to verify the presence of h^+. The results (Fig. 14a) indicated that no EPR signal was detected in the absence of light irradiation. However, after 5 min of exposure to light, the EPR spectrum of the methanol system exhibited distinct six-line spectra, whereas the aqueous system showed four-line signal peaks with a 1 : 2 : 2 : 1 ratio. These peaks corresponded to $\cdot O_2^-$ and ·OH trapped by DMPO, respectively.[70] In Fig. 14b, three 1 : 1 : 1 TEMPO signal peaks were observed, and upon light

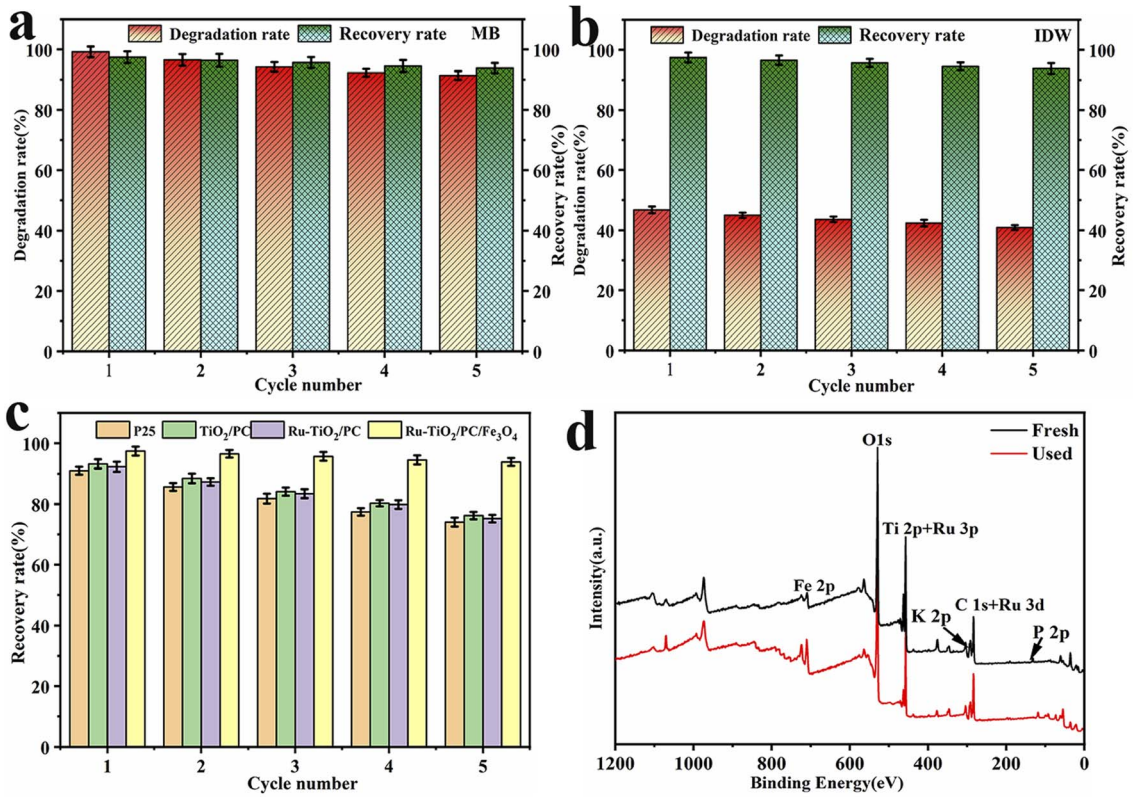

Fig. 13 Cycling stability and recyclability curves with error bars of Ru-TiO_2/PC/Fe_3O_4 samples: (a) MB dye solution, (b) IDW; (c) comparison of recyclability of different catalysts; (d) XPS spectra of PCTRF-100 before and after five cycles of reaction with MB solution.

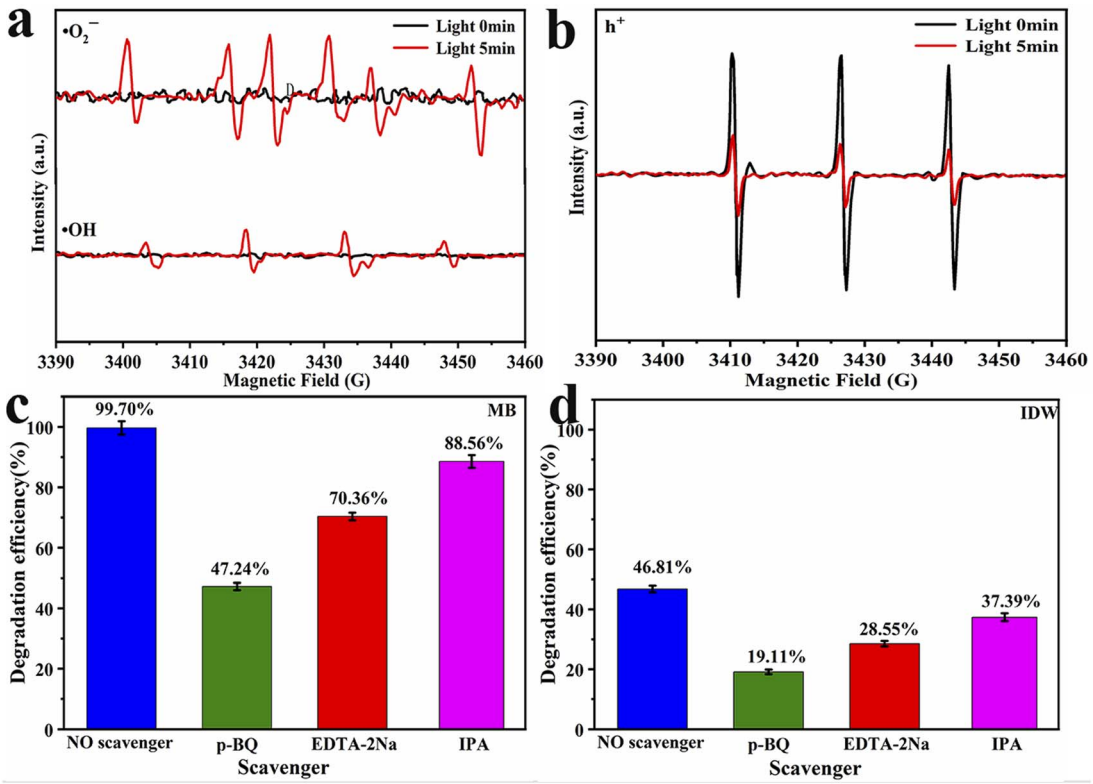

Fig. 14 EPR spectra of Ru-TiO_2/PC/Fe_3O_4 sample: (a) $\cdot O_2^-$ and ·OH; (b) h^+. Results of free radical trapping experiments with error bars: (c) MB; (d) IDW.

irradiation, a significant reduction in peak intensity was noted. This confirmed the generation of h^+ under light irradiation, as h^+ reacted with TEMPO, leading to a decrease in TEMPO signal intensity. This phenomenon aligns with previous research findings.[71] In summary, the Ru-TiO_2/PC/Fe_3O_4 composite catalyst is capable of generating active free radicals, such as $\cdot O_2^-$, ·OH, and h^+, under light irradiation, which are essential in the photocatalytic reaction process.

To further investigate the role of various free radicals in the photocatalytic process, radical trapping experiments were conducted in MB solution and IDW. *p*-Benzoquinone (*p*-BQ), ethylenediaminetetraacetic acid disodium salt (EDTA-2Na), and isopropanol (IPA) were employed as scavengers for $\cdot O_2^-$, h^+, and ·OH, respectively.[72,73] The results are presented in Fig. 14c and d. As depicted in the figures, the addition of *p*-BQ resulted in a reduction in the degradation rates of MB and IDW by 52.46% and 27.70%, respectively. Similarly, the introduction of EDTA-2Na led to decreases in degradation rates by 29.34% and 18.26%, respectively. When IPA was added, the degradation rates declined by 10.14% and 9.42%, respectively. These findings suggest that $\cdot O_2^-$ plays the most significant role in the photocatalytic process, followed by h^+, while the influence of ·OH is comparatively minor.

Based on the EPR analysis and the results of free radical trapping experiments, the mechanism of photocatalytic degradation of pollutants by the Ru-TiO_2/PC/Fe_3O_4 composite material is elucidated (Fig. 15). The superior photocatalytic performance of this composite material can be attributed to the synergistic effects of Ru-doped TiO_2, biochar, and Fe_3O_4. The doping of Ru reduces the bandgap energy of TiO_2, enabling its excitation under simulated solar light to produce electron–hole pairs. Furthermore, Ru doping introduces intermediate energy levels that facilitate electron transition and transport. Biochar, which contains graphitic carbon, exhibits good conductivity and functions as an electron acceptor, capturing electrons from the conduction band and intermediate energy levels, thereby promoting effective electron–hole separation. Additionally, the internal magnetic field of Fe_3O_4 nanoparticles modulates the electron transport pathways, effectively suppressing the recombination of electrons and holes. These synergistic interactions result in the retention of more e^- and h^+ within the reaction system.[74] The conduction band potential of Ru-TiO_2/PC/Fe_3O_4 (−0.74 eV) is lower than the reduction potential of O_2/$\cdot O_2^-$ (−0.33 eV), allowing e^- to react with O_2 on the material's surface to generate strongly oxidizing $\cdot O_2^-$. However, its valence band potential (+1.74 eV) is higher than the oxidation potential of ·OH/H_2O (+2.38 eV), preventing h^+ from directly oxidizing H_2O to ·OH. Both EPR tests and free radical trapping experiments confirm that ·OH is also one of the active species. It is speculated that ·OH is formed through the reaction of $\cdot O_2^-$ with H_2O, initially producing H_2O_2, which subsequently decomposes.[75] The combined action of $\cdot O_2^-$, ·OH, and h^+ degrades dye pollutants into colorless small molecules. The entire process can be described in detail through chemical eqn (1)–(7).[76]

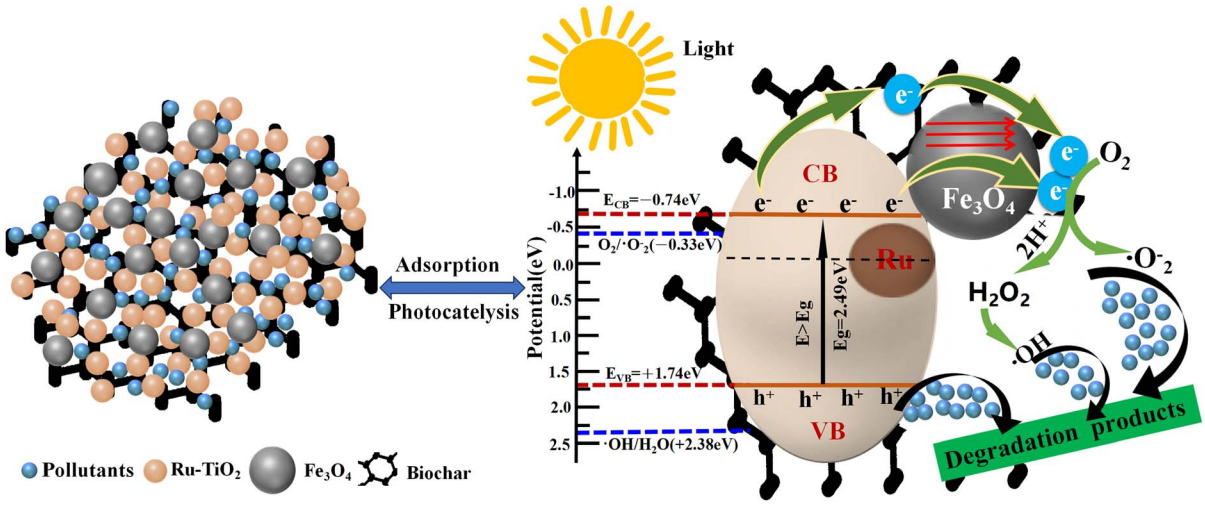

Fig. 15 Schematic diagram of the mechanism for photocatalytic degradation of organic pollutants by Ru-TiO_2/PC/Fe_3O_4 composite material.

$$\text{Ru-TiO}_2\text{/PC/Fe}_3\text{O}_4 + h\nu \rightarrow \text{h}^+ + \text{e}^-(\text{TiO}_2) \quad (1)$$

$$\text{e}^-(\text{TiO}_2) \rightarrow \text{e}^-(\text{PC, Ru}) \quad (2)$$

$$\text{e}^-(\text{Ru}) \rightarrow \text{e}^-(\text{PC}) \quad (3)$$

$$\text{O}_2 + \text{e}^-(\text{TiO}_2\text{, PC}) \rightarrow \cdot\text{O}_2^- \quad (4)$$

$$\text{O}_2 + 2\text{H}^+ + 2\text{e}^- \rightarrow \text{H}_2\text{O}_2 \quad (5)$$

$$\text{H}_2\text{O}_2 + \text{e}^- \rightarrow \text{OH}^- + \cdot\text{OH} \quad (6)$$

$$(\cdot\text{O}_2^-, \text{h}^+ \text{ and } \cdot\text{OH}) + \text{pollutants} \rightarrow \text{degraded products} \quad (7)$$

4 Conclusion

In this study, a series of Ru-TiO_2/PC/Fe_3O_4 composite materials with varying mass ratios was successfully synthesized, and their structures and physicochemical properties were thoroughly characterized using XRD, XPS, SEM, and TEM. The analysis revealed that Fe_3O_4 within the composite adopted a cubic spinel structure, characteristic of magnetite, while TiO_2 predominantly exhibited the anatase phase. It was found that Ru-TiO_2 and Fe_3O_4 nanoparticles were uniformly distributed on the GP biochar. The composite material demonstrated a large specific surface area, a narrow band gap, high photocurrent, and low electrochemical impedance. Photocatalytic studies demonstrate that the Ru-TiO_2/PC/Fe_3O_4 composite catalyst outperforms P25, Fe_3O_4/PC, and Ru-TiO_2/PC in degrading dye pollutants. The photocatalytic efficiency increases with the Fe_3O_4/PC content up to an optimal level, after which it declines, with PCTRF-100 exhibiting the highest performance. Under 600 W xenon lamp irradiation, PCTRF-100 achieved degradation rates of 99.4% and 99.8% for RhB and MB within 60 minutes, respectively, and 98.04% for MO within 120 minutes. Additionally, it demonstrated significant effectiveness in treating industrial dyeing wastewater, achieving a degradation rate of 46.82% within 300 minutes and reducing the COD value from 1540 mg L^{-1} to 784 mg L^{-1}. Furthermore, the composite material is easily separable and recyclable under a magnetic field, exhibiting excellent cycling stability. Analysis of the photocatalytic mechanism revealed that $\cdot O_2^-$ and h^+ were the primary active species generated during the photocatalytic process, while the synergistic interactions among Ru-TiO_2, biochar, and Fe_3O_4 effectively enhanced the separation efficiency of photogenerated electron–hole pairs, significantly improving photocatalytic performance. This study developed an efficient and recyclable photocatalyst from waste biomass, providing significant insights into its application in environmental remediation and related fields. Future research should focus on expanding the range of target pollutants, studying long-term stability, evaluating performance under natural sunlight, and integrating with advanced treatment technologies to further enhance its industrial application value.

Data availability

Data are available upon request from the authors.

Author contributions

Ruixiang wu (conceptualization; data curation; formal analysis; investigation; methodology; software; supervision; validation; writing – original draft; writing – review & editing). Hanyan Zhang (data curation; investigation; methodology; resources; validation). Wenhua Liu (conceptualization; funding acquisition; project administration; resources; supervision; writing – review & editing). Renao Bai (formal analysis; investigation). Delun Zheng (data curation; investigation; software). Xiufang Tian (data curation; investigation; methodology). Weikai Lin (data curation; investigation; software). Lejian Li (data curation; investigation; software). Qianwei Ke (data curation; investigation; software).

Conflicts of interest

There are no conflicts to declare.

Acknowledgements

We are grateful for the financial support from the Special Fund Project for Science and Technology Innovation Strategy of Guangdong Province (No. pdjh2021b0916).

References

1 S. S. Neetu, P. Srivastava and L. Bahadur, *Sol. Energy*, 2020, **208**, 173–181.
2 Q. Zhang, L. Y. Yu, B. R. Yang, C. C. Xu, W. Zhang, Q. Xu and G. W. Diao, *Chem. Phys. Lett.*, 2021, **774**, 138609.
3 R. Singh, M. Kumar, H. Khajuria, J. Ladol and H. N. Sheikh, *Chem. Pap.*, 2018, **72**, 1181–1192.
4 N. Soltani, E. Saion, M. Z. Hussein, M. Erfani, A. Abedini, G. Bahmanrokh, M. Navasery and P. Vaziri, *Int. J. Mol. Sci.*, 2012, **13**(10), 12242–12258.
5 C. A. D'Amato, R. Giovannetti, M. Zannotti, E. Rommozzi, S. Ferraro, C. Seghetti, M. Minicucci, R. Gunnella and A. Di Cicco, *Appl. Surf. Sci.*, 2018, **441**, 575–587.
6 R. Taourati, M. Khaddor, A. Laghzal and A. E. Kasmi, *Environ. Sci. Technol.*, 2020, **8**, e00305.
7 S. Q Chen, H. D. Liang, M. Shen and Y. X. Jin, *Appl. Phys. A: Mater. Sci. Process.*, 2018, **124**, 305.
8 H. R. Mardani, *Res. Chem. Intermed.*, 2017, **43**, 5795–5810.
9 P. K. Boruah, P. Borthakur, G. Darabdhara, C. K. Kamaja, I. Karbhal, M. V. Shelke, P. Phukan, D. Saikia and M. R. Das, *RSC Adv.*, 2016, **6**, 11049–11063.
10 C. Chen, Z. H. Ma, S. Y. Zhou, T. Q. Li and X. L. Sun, *Catal. Lett.*, 2017, **147**, 2399–2409.
11 K. S. Ranjith, P. Manivel, R. T. Rajendrakumar and T. Uyar, *Chem. Eng. J.*, 2017, **325**, 588–600.
12 H. R. Chen, K. Shen, J. Y. Chen, X. D. Chen and Y. W. Li, *J. Mater. Chem. A*, 2017, **5**, 9937–9945.
13 B. Uzunbayir, U. Kartal, E. C. Doluel, M. Yurddaskal and M. Erol, *J. Sol-Gel Sci. Technol.*, 2020, **96**(2), 441–451.
14 T. T. Qian, X. P. Yin, J. H. Li, H. E. Nian, H. Xu, Y. Deng and X. Wang, *J. Mater. Sci. Technol.*, 2017, **33**(11), 1314–1322.
15 T. Hariff, M. Montazer, R. Dillert and D. W. Bahnemann, *J. Clean. Prod.*, 2018, **196**, 688–697.
16 Z. Y. Zhang, C. C. Zhao, Y. S. Duan, C. Wang, Z. C. Zhao, H. J. Wang and Y. J. Gao, *Appl. Surf. Sci.*, 2020, **527**, 146693.
17 S. Khammar, N. Bahramifar and H. Younesi, *J. Hazard. Mater.*, 2020, **394**, 122422.
18 P. P. Chen, Y. Y. Cai, J. Wang, K. W. Wang, Y. S. Tao, J. D. Xue and H. G. Wang, *Powder Technol.*, 2018, **326**, 272–280.
19 R. X. Wu, W. H. Liu, R. A. Bai, X. F. Tian, W. K. Lin, L. J. Li and Q. W. Ke, *RSC Adv.*, 2024, **14**, 15604–15618.
20 R. X. Wu, W. H. Liu, R. A. Bai, D. L. Zheng, X. F. Tian, W. K. Lin, Q. W. Ke and L. J. Li, *Molecules*, 2024, **29**(9), 2090.
21 R. M. Kulkami, R. S. Malladi, M. S. Hanagadakar, M. R. Doddamani, B. Santhakumari and S. D. Kulkarni, *J. Mater. Sci.: Mater. Electron.*, 2016, **27**(12), 13065–13074.
22 R. A. Elsalamony and S. A. Mahmoud, *Arab. J. Chem.*, 2017, **10**(2), 194–205.
23 H. B Zhang, S. W. Zuo, M. Qiu, S. B. Wang, Y. F. Zhang and X. W. Lou, *Sci. Adv.*, 2020, **6**(39), abb9823.
24 N. I. Mohd Razip, K. M. Lee, C. W. Lai and B. H. Ong, *Mater. Res. Express*, 2019, **6**(7), 075517.
25 A. C. Sun, *Adv. Powder Technol.*, 2018, **29**(3), 719–725.
26 H. L. Niu, Q. M. Wang, H. X. Liang, M. Chen, C. J. Mao, J. M. Song, S. Y. Zhang, Y. H. Gao and C. Chen, *Materials*, 2014, **7**(5), 4034–4044.
27 Q. Zhang, L. Y. Yu, C. C. Xu, J. Y. Zhao, H. Y. Pan, M. Chen, Q. Xu and G. W. Diao, *Appl. Surf. Sci.*, 2019, **483**, 241–251.
28 J. R. Rajabathar, R. Thankappan, A. Sutha, H. Al-Lohedan, A. M. Karami, S. A. Kumar, G. Devendrapandi, S. R. Marjorie and R. Balu, *Opt. Mater.*, 2024, **148**, 114820.
29 H. X. Huang, T. Guo, K. Wang, Y. Li and G. K. Zhang, *Sci. Total Environ.*, 2021, **758**, 143957.
30 Z. Y. Zhang and J. L. Kong, *J. Hazard. Mater.*, 2011, **193**, 325–329.
31 B. Y. Wang, M. Zhang, W. Z. Li, L. L. Wang, J. Zheng, W. J. Gan and J. L. Xu, *Dalton Trans.*, 2015, **44**, 17020–17025.
32 Z. Y. Zhang, Z. Y. Xiong, C. C. Zhao, P. J. Guo, H. J. Wang and Y. J. Gao, *Appl. Surf. Sci.*, 2021, **565**, 150554.
33 R. Djellabi, B. Yang, Y. Wang, X. Q. Cui and X. Zhao, *Chem. Eng. J.*, 2019, **366**, 172–180.
34 T. Rajaramanan, M. Natarajan, P. Ravirajan, M. Senthilnanthanan and D. Velauthapillai, *Energies*, 2020, **13**(7), 1532.
35 M. Ismael, *New J. Chem.*, 2019, **43**, 9596–9605.
36 M. M. Shi, D. Bao, S. J. Li, B. R. Wulan, J. M. Yan and Q. Jiang, *Adv. Energy Mater.*, 2018, **8**(21), 1800124.
37 Y. Y. Cao, G. H. Shen, Y. Zhang, C. F. Gao, Y. F. Li, P. Z. Zhang, W. H. Xiao and L. J. Han, *Sci. Total Environ.*, 2019, **692**, 479–489.
38 Y. Ling, M. Zhang, X. K Li, J. Zheng and J. L. Xu, *Dalton Trans.*, 2018, **47**, 10093–10101.
39 H. F. Zhuang, H. Zhu, J. Zhang, S. D. Shan, C. G. Fang, H. J Tang and Q. N. Xie, *Bioresour. Technol.*, 2020, **296**, 122306.
40 B. Sun, N. Lu, Y. Su, H. T. Yu, X. Y. Meng and Z. M. Gao, *Appl. Surf. Sci.*, 2017, **394**, 479–487.
41 Y. G. Tan, Z. Shu, J. Zhou, T. T. Li, W. B. Wang and Z. L. Zhao, *Appl. Catal., B*, 2018, **230**, 260–268.
42 A. A. Gonçalves, P. C. Siciliano, O. C. Alves, D. V. Cesar and C. A. Henriques, *Top. Catal.*, 2020, **63**(14), 1017–1029.
43 D. L. Qian, D. Y. Chen, N. J. Li, Q. F. Xu, H. Li, J. H. He and J. M. Lu, *J. Membr. Sci.*, 2018, **554**, 16–25.
44 D. Li, X. L. Guo, H. R. Song, T. Y. Sun and J. F. Wan, *J. Hazard. Mater.*, 2018, **351**, 250–259.
45 X. H. Jia, R. R. Dai, D. D. Lian, S. Han, X. Y. Wu and H. J. Song, *Appl. Surf. Sci.*, 2017, **392**, 268–276.
46 L. J. Duan, N. Jiang, N. Lu, K. F. Shang, J. Li and Y. Wu, *Appl. Catal., B*, 2018, **221**, 521–529.
47 J. N. Li, Q. C. Zhang, J. M. Liu, M. R. Yu, H. Y. Ma, J. C. Yang, S. Ye, T. R. Reina and J. Liu, *J. Colloid Interface Sci.*, 2020, **577**, 512–522.
48 S. Banerjee, P. Benjwal, M. Singh and K. K. Kar, *Appl. Surf. Sci.*, 2018, **439**, 560–568.
49 S. Wang, B. Liu, Y. Zhu, Z. R. Ma, B. B. Liu, X. Miao, R. X. Ma and C. Y. Wang, *Sol. Energy*, 2018, **169**, 335–342.
50 H. H. Li, Z. Q. Jin, N. Lu, J. M. Pan, J. L. Xu, X. B. Yin and M. Zhang, *Dalton Trans.*, 2024, **53**, 6974.

51 X. L. Wang, M. W. Zhang, J. M. Zhao, G. Y. Huang and H. Y. Sun, *Appl. Surf. Sci.*, 2018, **427**, 1054–1063.
52 C. Y. Kuo, C. H. Wu, J. T. Wu and Y. R. Chen, *React. Kinet. Mech. Catal.*, 2015, **114**, 753–766.
53 S. F. Zhao, Y. J. Ji, M. Jeong, H. Choe, J. W. Lee, S. Y. Kim, S. Saqlain, Z. K. Peng, Z. Y. Liu and Y. D. Kim, *Chem. Eng. J.*, 2022, **444**, 136500.
54 W. B. Chai, X. Y. Liu, J. C. Zou, X. Y. Zhang, B. B. Li and T. T. Yin, Pomelo peel modified with acetic anhydride and styrene as new sorbents for removal of oil pollution, *Carbohydr. Polym.*, 2015, **132**, 245–251.
55 S. O. Dan and S. H. Khan, An Overview on Green Titanium Nanoparticles Based on Plants: Synthesis, Potential Applications and Eco-Friendly Approach, *Int. J. Life Sci. Biotechnol. Pharma Res.*, 2022, **12**(5), 215–P233.
56 Y. Zhou, S. R. Cao, C. X. Xi, X. L. Li, L. Zhang, G. M. Wang and Z. Q. Chen, A novel Fe3O4/graphene oxide/citrus peel-derived bio-char based nanocomposite with enhanced adsorption affinity and sensitivity of ciprofloxacin and sparfloxacin, *Bioresour. Technol.*, 2019, **292**, 121951.
57 E. Grabowskaa, M. Diak, T. Klimczuk, W. Lisowski and A. Z. Medynska, Novel decahedral TiO_2 photocatalysts modified with Ru or Rh NPs: Insight into the mechanism, *Mol. Catal.*, 2017, **434**, 154–166.
58 Y. Zhou, S. R. Cao, C. X. Xi, X. L. Li, L. Zhang, G. M. Wang and Z. Q. Chen, *Bioresour. Technol.*, 2019, **292**, 121951.
59 E. Grabowskaa, M. Diak, T. Klimczuk, W. Lisowski and A. Z. Medynska, *Mol. Catal.*, 2017, **434**, 154–166.
60 Y. F. Liu, L. J. Wang, X. W. Dai, J. Zhang, J. Li and Y. B. Ma, *J. Alloys Compd.*, 2024, **976**, 172985.
61 B. Mercyrani, R. H. Maya, M. S. López, C. T. Th and S. Velumani, *J. Mater. Sci.: Mater. Electron.*, 2018, **29**(18), 15436–15444.
62 Y. M. Hunge, A. A. Yadav, S. Khan, K. Takagi, N. Suzuki, K. Teshima and C. Terashima, *J. Colloid Interface Sci.*, 2021, **582**, 1058–1066.
63 Y. Jiang and A. Liu, *Environ. Sci. Pollut. Res. Int.*, 2023, **30**, 31923–31934.
64 Y. J. Yang, Y. Yao, L. He, Y. T. Zhong, Y. Ma and J. N. Yao, *J. Mater. Chem. A*, 2015, **3**, 10060–10068.
65 J. T. Zhang, Y. H. Cao, P. Zhao, T. F. Xie, Y. H. Lin and Z. Mu, *Colloids Surf., A*, 2020, **601**, 125019.
66 Z. Y. Chen, W. W. P. Lai, H. H. H. Lin, J. X. Tan, K. C. W. Wu and A. Y. C. Lin, *J. Environ. Chem. Eng.*, 2022, **10**, 108637.
67 L. Zhu, X. Q. Kong, C. W. Yang, B. X. Ren and Q. Tang, *J. Hazard. Mater.*, 2020, **381**, 120910.
68 X. N. Wei and H. L. Wang, *J. Alloys Compd.*, 2018, **763**, 844–853.
69 Q. Z. Mu, Y. F. Sun, A. Y. Guo, X. Z. Yu, X. Y. Xu, A. J. Cai and X. P. Wang, *Mater. Res. Express*, 2019, **6**, 0950c3.
70 Y. Liu, J. F. Wan, C. T. Liu and Y. B. Li, *Mater. Sci. Technol.*, 2016, **32**(8), 1743284715y.
71 M. Gebrezgiabher, G. Gebreslassie, T. Gebretsadik, G. Yeabyo, F. Elemo, Y. Bayeh, M. Thomas and W. Linert, *J. Compos. Sci.*, 2019, **3**(3), 75.
72 S. N. Zhuo, H. Y. Ren, G. L. Cao, G. J. Xie, D. F. Xing, N. Q. Ren and B. F. Liu, *Chem. Eng. J.*, 2022, **440**, 135947.
73 Z. H. Li, H. Bai, J. L. Wei, J. J. Wang, L. L. Kong, X. Wang, X. D. Xia and J. Y. Duan, *J. Colloid Interface Sci.*, 2022, **610**, 893–904.
74 W. D. Dai, L. Jiang, J. Wang, Y. J. Pu, Y. F. Zhu, Y. X. Wang and B. B. Xiao, *Chem. Eng. J.*, 2020, **397**, 125476.
75 S. Q. Wu, X. Y. Li, Y. Q. Tian, Y. Lin and Y. H. Hu, *Eng. J.*, 2021, **406**, 126747.
76 J. H. Tan, X. Wang, W. S. Hou, X. L. Zhang, L. Q. Liu, J. H. Ye and D. F. Wang, *J. Alloys Compd.*, 2019, **792**, 918e927.